



THE MOLECULAR WIND IN THE NEAREST SEYFERT GALAXY CIRCINUS REVEALED BY ALMA

Laura K. Zschaechner¹, Fabian Walter¹, Alberto Bolatto², Emanuele P. Farina¹, J. M. Diederik Kruijssen^{1,3}, Adam Leroy^{4,5}, David S. Meier⁶, Jürgen Ott⁷, and Sylvain Veilleux²

¹Max Planck Institute für Astronomie—Königstuhl 17, D-69117 Heidelberg, Germany; zschaechner@mpia.de

²Department of Astronomy and Joint Space Science Institute, University of Maryland, College Park, MD 20642, USA

³Astronomisches Rechen-Institut, Zentrum für Astronomie der Universität Heidelberg, Mönchhofstraße 12-14, D-69120 Heidelberg, Germany

⁴Department of Astronomy, The Ohio State University, 140 West 18th Avenue, Columbus, OH 43210, USA

⁵National Radio Astronomy Observatory, 520 Edgemont Road, Charlottesville, VA 22903, USA

⁶Department of Physics, New Mexico Institute of Mining and Technology, 801 Leroy Place, Socorro, NM 87801, USA

⁷National Radio Astronomy Observatory—P.O. Box O, 1003 Lopezville Road, Socorro, NM 87801, USA

Received 2016 July 26; revised 2016 September 13; accepted 2016 September 14; published 2016 November 28

ABSTRACT

We present ALMA observations of the inner 1' (1.2 kpc) of the Circinus galaxy, the nearest Seyfert. We target CO (1–0) in the region associated with a well-known multiphase outflow driven by the central active galactic nucleus (AGN). While the geometry of Circinus and its outflow make disentangling the latter difficult, we see indications of outflowing molecular gas at velocities consistent with the ionized outflow. We constrain the mass of the outflowing molecular gas to be 1.5×10^5 – $5.1 \times 10^6 M_{\odot}$, yielding a molecular outflow rate of 0.35 – $12.3 M_{\odot} \text{ yr}^{-1}$. The values within this range are comparable to the star formation (SF) rate in Circinus, indicating that the outflow indeed regulates SF to some degree. The molecular outflow in Circinus is considerably lower in mass and energetics than previously studied AGN-driven outflows, especially given its high ratio of AGN luminosity to bolometric luminosity. The molecular outflow in Circinus is, however, consistent with some trends put forth by Cicone et al., including a linear relation between kinetic power and AGN luminosity, as well as its momentum rate versus bolometric luminosity (although the latter places Circinus among the starburst galaxies in that sample). We detect additional molecular species including CN and C¹⁷O.

Key words: galaxies: individual (Circinus) – galaxies: Seyfert – galaxies: star formation – Galaxy: evolution – ISM: jets and outflows – molecular data

1. INTRODUCTION

A primary source of feedback in galaxies is galactic outflows/winds (Veilleux et al. 2005). They potentially expel material into the intergalactic medium (IGM), enriching the surrounding environment and constituting a reservoir of material that can be reaccreted to fuel later star formation (SF) in galaxies (Oppenheimer et al. 2010). Galactic winds also play an important role in driving bubbles into the ISM that allow radiation to propagate further (Dove et al. 2000). Galactic winds are invoked to explain the observed paucity of massive galaxies in the local universe (e.g., Somerville et al. 2008) and the quenching of SF in massive galaxies (e.g., Barai et al. 2013). Thus, it is imperative to gauge the total outflow rate and compare it to the accretion rate in order to understand the evolution of galaxies. While a recent emphasis has been placed on researching galactic winds (e.g., Veilleux et al. 2005; Feruglio et al. 2010; Sharp & Bland-Hawthorn 2010; Bolatto et al. 2013a; Cicone et al. 2014; Aalto et al. 2015; Alatalo et al. 2015), the degree to which they regulate evolutionary processes is still poorly constrained, largely due to insufficient observational data. With the advent of instruments such as ALMA, the molecular phases of galactic winds may now be mapped in detail and with superb velocity resolution.

A fundamental question is the relative importance of starburst- and active galactic nucleus (AGN)-driven winds in the feedback process. Both tend to suppress SF by removing molecular gas, but the efficiency with which they do so is unknown. Both affect the surrounding ISM, but their respective impacts may differ based on their energetics and distributions within the host galaxies. Simulations and observations indicate that AGN-driven winds are more energetic and concentrated

near the center, resulting in a higher chance for material to escape the galaxy and a lower likelihood of it fueling future SF (Sharma & Nath 2012). Starburst-driven winds, however, are more widely distributed and may eject material at larger galactocentric radii, producing a greater effect on the ISM. When both are present, the two types of outflows may work to amplify their respective contributions (Pawlik & Schaye 2009), but can also counteract each other's effects (Booth & Schaye 2013). Fundamentally, their impact depends on their efficiency at entraining and ejecting material of the various phases of the ISM from the disk.

Molecular outflows are seen in several starburst galaxies, including M82 (Walter et al. 2002; Leroy et al. 2015b), Arp 220 (Sakamoto et al. 2009), NGC 253 (Bolatto et al. 2013a), and NGC 1808 (Salak et al. 2016) among others. The molecular mass outflow rates in these galaxies indicate that starburst-driven molecular outflows can indeed regulate SF, particularly in NGC 253 where the molecular mass outflow rate was determined to be >3 times the global star formation rate (SFR) in that galaxy, and likely higher.

During the past five years there have been a number of studies focusing on AGN-driven outflows, summarized in Sturm et al. (2011), Veilleux et al. (2013), Cicone et al. (2014), Feruglio et al. (2015), and Leroy et al. (2015a). These studies show that an increase in AGN luminosity (L_{AGN}) typically results in stronger outflows, with some reaching values of over $1000 M_{\odot} \text{ yr}^{-1}$ for the molecular component. There are also indications that stronger outflows may also be tied to a high ratio of L_{AGN} to the bolometric luminosity (L_{bol}), but that appears to be less important.

Other results by Alatalo et al. (2015) indicate a molecular outflow of $\sim 100 M_{\odot} \text{ yr}^{-1}$ with an average velocity of 177 km s^{-1} within a radius of $\sim 225 \text{ pc}$ in NGC 1266, and Aalto et al. (2016) determine a molecular mass outflow rate for NGC 1377 of $9\text{--}30 M_{\odot} \text{ yr}^{-1}$, showing a strong jet potentially entraining the cold gas extending out to $\sim 150 \text{ pc}$ in projection, with velocity estimates from 240 to 850 km s^{-1} . Morganti et al. (2015) and Tadhunter et al. (2014) characterize the AGN-driven molecular outflow in IC 5063, a radio-weak Seyfert galaxy where the multiphase outflow components (ionized, H I, warm H_2 , cold molecular gas) share similar kinematics. The molecular mass outflow rate they determine is sufficiently high and the AGN sufficiently weak that the radio jet within that galaxy is likely the primary driver of the outflow—not radiation from the AGN. However, in Mrk 231, Morganti et al. (2016) find that it is unlikely that a jet is driving its multiphase (Na I, H I, OH, and CO) outflow.

In contrast to those massive molecular outflows, Matsushita et al. (2007) detect a more modest molecular outflow of $\sim 4 M_{\odot} \text{ yr}^{-1}$ in M51—a galaxy that is neither starbursting nor a ULIRG. They conclude that the molecular outflow is likely mechanically driven by a radio jet as opposed to SF (which is spread throughout the disk) or radiation from the AGN (which is too weak). The bulk of the molecular outflow they detect is within $1''$ (34 pc) of the center of M51—quite small by comparison to the molecular outflows observed in other systems and unlikely to impact SF throughout M51. Combes et al. (2014) observe NGC 1566, a galaxy with a low-luminosity AGN, with ALMA and find no evidence for a molecular outflow or AGN-driven feedback.

In the current sample of molecular outflows there appears to be a correlation between AGN luminosity and powerful outflows. As noted in Ciccone et al. (2014), however, there is a bias in that, with a few exceptions (e.g., ULIRGs in the Herschel sample presented in Sturm et al. 2010 for which the molecular outflows were investigated by Veilleux et al. 2013), only galaxies with previously detected, high-velocity molecular outflows are considered. It is necessary to observe molecular outflows in host galaxies with a range of AGN luminosities at high spatial resolution in order to see if these trends hold.

1.1. The Circinus Galaxy

At an adopted distance of 4.2 Mpc ($1'' = 20.4 \text{ pc}$, Tully et al. 2009), the nearest Seyfert 2 (Oliva et al. 1994) is The Circinus galaxy (Freeman et al. 1977). An ionized outflow is clearly observed emerging from the nuclear region of Circinus, with blueshifted velocities (receding components are likely obscured by the intervening disk) of approximately -150 km s^{-1} (e.g., Marconi et al. 1994; Veilleux & Bland-Hawthorn 1997; Wilson et al. 2000, Figure 1). The ionized component extends for at least $30''$ along the minor axis and farther. Veilleux & Bland-Hawthorn (1997) also observe what look like bow-shocked features resembling Herbig–Haro objects at the ends of these filaments suggesting a strong interaction with the surrounding ISM. Elmouttie et al. (1998) detect an outflow in the radio continuum, most prominently in the northwestern direction, but with a counter-jet to the southeast. This counter-jet shows that the outflow is not entirely one-sided, and observations of the molecular phase (which suffers less from extinction effects) may indeed uncover a counter-jet closer to the disk—a possibility we explore in this work. Observational parameters of Circinus are listed in Table 1.

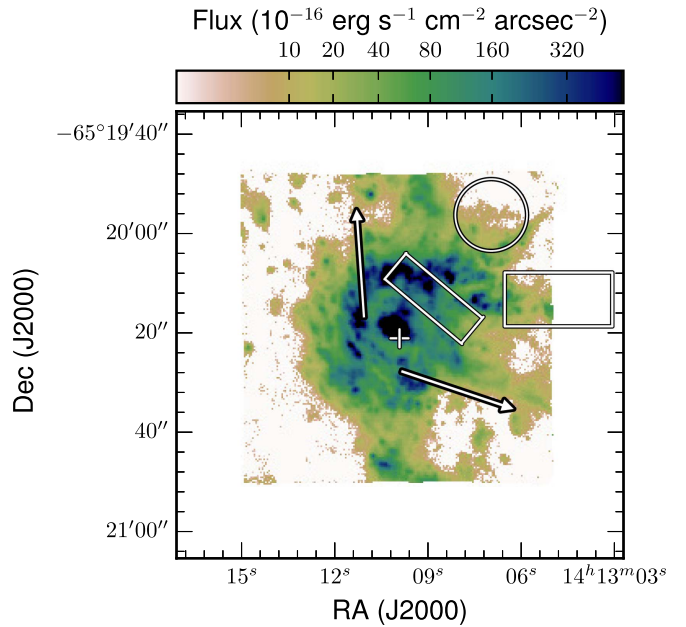


Figure 1. $\text{H}\alpha$ image of Circinus created with MUSE data (full presentation of the MUSE data in Marconi et al. 2016, in preparation, and Venturi et al. 2016, in preparation). Multiple filaments extend from the central regions of the disk (center marked with a cross). The approximate width of the $\text{H}\alpha$ outflow cone is shown by the two large arrows. Regions referred to throughout the text are introduced here for reference although their molecular components are not visible. The slanted rectangle near the center marks the molecular “overdense region,” the circle marks the “NW cloud,” and the rectangle to the west marks the “far W cloud.” Assuming our adopted distance of 4.2 Mpc , $1'' = 20.4 \text{ pc}$.

Table 1
The Circinus Galaxy

Parameter	Value	Reference
Distance	4.2 Mpc	Tully et al. (2009)
SFR	$4.7 M_{\odot} \text{ yr}^{-1}$	Zhu et al. (2008) ^a
L_{bol}	$1.7 \times 10^{10} L_{\odot}$	Maiolino et al. (1998) ^b
L_{AGN}	$10^{10} L_{\odot}$	Moorwood et al. (1996)
Type	Seyfert 2	Oliva et al. (1994)
Black hole mass	$1.7 \times 10^6 \pm 0.3 M_{\odot}$	Greenhill et al. (2003)
Eddington luminosity	$5.6 \times 10^{10} L_{\odot}$	Tristram et al. (2007)

Notes.

^a Multiple values from the literature for the star formation rate are listed in For et al. (2012). We adopt the value derived using L_{TIR} .

^b Originally derived by Siebenmorgen et al. (1997) and modified by Maiolino et al. (1998).

This paper is organized as follows. In Sections 2–3 we present the observations, calibration, and the data. In Section 4 we present our analysis and results followed by a discussion in Section 5. We provide a summary of our results in Section 6. The Appendix includes details of our kinematic modeling.

2. OBSERVATIONS AND DATA REDUCTION

In order to study the molecular outflow in Circinus, we mapped the inner $1'$ (1.2 kpc) in the CO (1–0) emission line (rest frequency 115.27120 GHz) with ALMA. These observations include additional frequencies from 99.8 to 115.7 GHz . The velocity resolution of our data is $2.5\text{--}3 \text{ km s}^{-1}$ over this frequency range. Our observational setup consisted of a seven-pointing mosaic with the 12 m array, a three-pointing mosaic

Table 2
Observational and Instrumental Parameters

Parameter	Value
Observation dates—ACA	2014 Jul 02 2014 Aug 10 2014 Aug 11
Observation dates—12 m Array	2014 Dec 27
Observation dates—Total Power Array	2015 Jan 14 2015 Jan 15 2015 Jan 17 2015 Jan 27 2015 Jan 31
Number of antennas ACA	10
Number of antennas 12 m	36
Pointing center	14 ^h 13 ^m 09 ^s .9 −65 ^d 20 ^m 21 ^s .0
Calibrators ACA—flux	Mars
Gain	J1617–5848
Bandpass	J1308–6707
Calibrators 12 m—flux	Ceres
Gain	J1227–6509
Bandpass	J1427–4206
Calibrator TP—all	J1424–6807
Channel Spacing—full bandwidth	976.562 kHz
Channel Spacing—individual line cubes	3.0 km s ^{−1}
Total bandwidth	7.5 GHz
Frequencies covered	99.8–103.5 GHz 111.9–115.7 GHz
Spatial resolution/beam size	2″–3″ 40–60 pc
rms noise (SPW 2 99.8 to 101.7 GHz)	1.8 mJy beam ^{−1}
(SPW 3 101.6 to 103.5 GHz)	1.9 mJy beam ^{−1}
(SPW 1 111.9 to 113.9 GHz)	2.4 mJy beam ^{−1}
(SPW 0 113.7 to 115.7 GHz)	3.0 mJy beam ^{−1}
(CO (1–0) line cube)	5.4 mJy beam ^{−1}
(CN (1–0), $J = 1/2$ line cube)	2.8 mJy beam ^{−1}
(CN (1–0), $J = 3/2$ line cube)	3.3 mJy beam ^{−1}

for the ALMA Compact Array (ACA), and single-pointing Total Power (TP) observations. Observing dates, times, and calibrators are listed in Table 2.

ALMA data are from programme ID: ADS/JAO.ALMA#2013.1.00247.S, PI: Zschaechner. Calibration of the ALMA data was done using the Common Astronomy Software Application (CASA). Initial calibration utilized the scripts provided by the ALMA staff for the ACA data and the ALMA pipeline for the 12 m data. Minor adjustments were made to the ACA calibration. Minor phase errors in the final cubes were eliminated via a single iteration of phase-only self-calibration on the 12 m data. Amplitude self-calibration was attempted but yielded no clear improvement and was not used.

Two sets of cubes were created: one set containing the full bandwidth of each spectral window (full spectral resolution), and another set containing each detected line (3 km s^{−1} spectral resolution). Cubes were created using both natural and Briggs weighting (Briggs 1995) with a robust parameter of 0.5 in order to maximize sensitivity and resolution, respectively. Masks based on naturally weighted cubes with thresholds of 3 σ were used to create clean boxes for the individual line cubes. The only exception was for the the CO (1–0) cube which, due to substantially brighter emission and larger radial extent, required a 6 σ mask (based on the naturally weighted cube) to remove artefacts. While using that mask, the final Briggs-

weighted cube was cleaned down to 4 σ , which was optimal for detecting the most flux while avoiding additional low-level artefacts. The cubes were then combined with data from the total power array using FEATHER. The final cube parameters are given in Table 2. The beam size is approximately 3 × 2″ for the naturally weighted cubes, and 2.7 × 2″.1 for the CO (1–0) Briggs-weighted cube which we present for all CO (1–0) maps. Representative channel maps of the CO (1–0) line are shown in Figure 3.

Integral-field spectroscopic data of the Circinus galaxy were collected during 2015 March 11 with the Multi-Unit Spectroscopic Explorer (MUSE, Bacon et al. 2010) on the ESO/VLT (programme ID: 094.B-0321(A), PI: Marconi). The seeing during the 4 × 500 s science exposures was mostly sub-arcsecond with small variations between 0″.85 to 1″.05. The MUSE data reduction pipeline (version 1.0.1) was used to perform standard steps of the data processing (Weilbacher et al. 2012, 2014). These steps included bias, flat field, illumination corrections, wavelength, and flux calibrations (using observations of the standard star EG274 collected in same night of the science images). The galaxy fills the MUSE field of-view (1′ × 1′). Before combining the single exposures, a sky model was created and subtracted from 4 × 100 s exposures of mostly empty sky fields taken between the science images. Finally, single exposures were sampled on the typical 0″.2 × 0″.2 × 1.25 Å grid and then combined. Wavelength calibration was refined in post-processing using the centroid of bright sky emission lines. This procedure results in an accuracy of better than one-tenth of a pixel.

3. THE DATA

ALMA detects bright molecular emission across Circinus with a typical spectrum shown in Figure 2. The continuum has a slight downward slope with increasing frequency and is on the order of 0.05 mJy bm^{−1} as shown in Figure 2. There appear to be no lines detected from 100 to 103.5 GHz. Prominent lines appear between 112 and 115.5 GHz, including CO (1–0), CN (1–0)—both $J = 1/2$ and $J = 3/2$ groups of hyperfine transitions, and C¹⁷O. A summary of the detected lines is given in Table 3.

The most prominent line throughout the spectrum is CO (1–0), which is the primary focus of this paper (Figure 3). Moment maps are created using software described in Serra et al. (2015) in order to retain faint emission. Figure 4 (left panel) shows moment maps of the CO (1–0) line. The integrated intensity (zeroth-moment) map shows a relatively symmetric main disk, with spiral arms extending to the northeast and southwest at both large and small radii. A moderate overdensity is present in the northwestern half of the galaxy (henceforth referred to as the overdense region).

The intensity-weighted velocity (first-moment) map (Figure 4, middle panel) shows that the disk has a well-behaved rotation curve peaking at ~200 km s^{−1} (deprojected), with the primary departures from circular rotation being in the two outer spiral arms and to the south. Interestingly, to match the observed velocities of the outer spiral arms without introducing radial motions, their rotational velocities would need to go to zero. This effect is likely produced via a combination of projection effects and streaming motions.

The intensity-weighted velocity dispersion (second-moment) map (Figure 4, right panel) shows substantial structure throughout the disk. There is a disturbance to the southwest

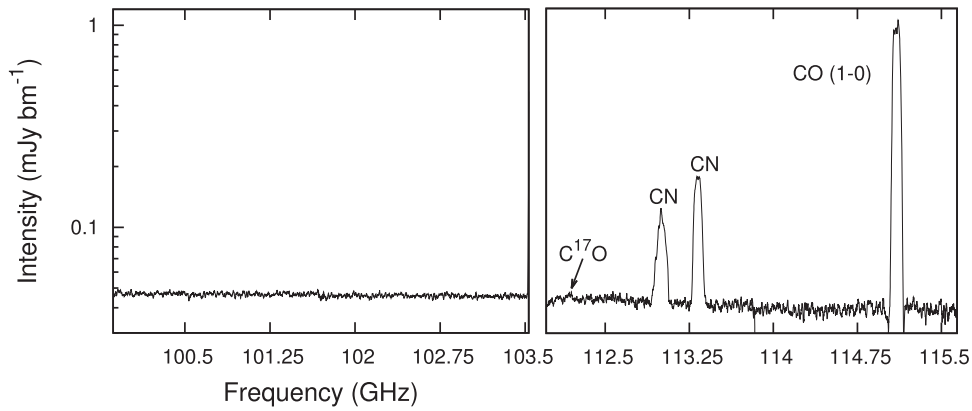


Figure 2. Full spectrum of all four spectral windows taken at the center of Circinus (left: lower sideband, right: upper sideband). Note the logarithmic scale. The CO (1–0) line appears prominently near 115 GHz, while the CN (1–0) $J = 1/2$ and $J = 3/2$ hyperfine structure lines are detected near 113 GHz. $C^{17}O$ is also detected in the center (peaking at 8 mJy bm^{-1} in a 3 km s^{-1} channel). The average beam for this spectrum is $2''.5$ and the values shown are taken at the pixel corresponding to the central pointing.

Table 3
Additional Molecular Species

Observed Frequency (GHz)	Molecular Species	Rest Frequency (GHz)
112.95 ^a	CN(1–0), $J = 1/2-1/2$, $F = 1/2-1/2$	113.123
112.98	$F = 1/2-3/2$	113.144
113.00	$F = 3/2-1/2$	113.170
113.01	$F = 3/2-3/2$	113.191
113.30–113.33	CN(1–0), $J = 3/2-1/2$, $F = 3/2-1/2$	113.488
113.30–113.33	$F = 5/2-3/2$	113.491
113.30–113.33	$F = 1/2-1/2$	113.500
113.30–113.33	$F = 3/2-3/2$	113.509
113.30–113.33	$F = 1/2-3/2$	113.520
112.18	$C^{17}O$	112.359

Note.

^a Taken from peak central position.

(henceforth referred to as the “southern disturbance”) with high velocity dispersion that goes approximately along the major axis and to the end of the outer spiral arm. The two spiral arms show an increased dispersion, especially directly along the edge of the main disk. To the north there is an abrupt decrease in the velocity dispersion when meeting the spiral arm, as well as a sudden change in velocity (first-moment map). Naturally, the dispersion near the center is expected to be high, but note here the increased dispersion in the overdense region noted in the integrated intensity map—consistent with a wind driven from the center. A similar increase in dispersion is not present to the southeast (azimuthally opposite region).

3.1. Likely Outflowing Molecular Gas

Most emission that is likely to be part of a molecular outflow is located northwest of the center in the aforementioned overdense region approximately $7''.5-15''$ or 330–650 pc as it extends along the minor axis (Figure 4). The molecular outflow itself is most readily seen as an increase in velocity dispersion. A typical value for the velocity dispersion of the clumpy disk gas is $\leq 10 \text{ km s}^{-1}$, while a higher dispersion ($\sim 15 \text{ km s}^{-1}$) diffuse

component is observed in some galaxies (e.g., Caldú-Primo et al. 2013; Caldú-Primo & Schrub 2016). In Circinus, the velocity dispersion in the overdense region is $30-50 \text{ km s}^{-1}$, which is shown more quantitatively in Figure 5.

There is also an extension to the northwest (referred to as the “NW cloud” in the text and circled in figures). The NW cloud is almost certainly associated with the outflow as it appears to be moving radially outward in projection in addition to being in apparent alignment with the ionized outflow cone. Its velocity is also blueshifted up to $\sim 150 \text{ km s}^{-1}$, similar to that of the ionized outflow. The overdense region and projected direction of the NW cloud coincide with the center of the outflow cone observed in the ionized gas (e.g., Marconi et al. 1994; Veilleux & Bland-Hawthorn 1997; Sharp & Bland-Hawthorn 2010).

There is a second extension to the west (referred to as “far W cloud” in the text and is encompassed by the western rectangle in figures). Like the NW cloud, the far W cloud is beyond the northern spiral arm and appears to travel radially outward from Circinus. The far W cloud also appears to extend along one of the $H\alpha$ filaments (Figure 6, 400 km s^{-1}). Furthermore, the far W cloud and the $H\alpha$ filament coincide in velocity.

Channel maps showing the NW and far west clouds are shown in Figure 7. In these channel maps, the NW cloud moves in a northwest direction with increasing velocity (inside the white circle). While there is nearby emission from the northern spiral arm in these channels, it is essential to note that, although the morphology changes somewhat between channels, there is no such spatial shift in the northwest direction by the arm emission. Thus, while the NW cloud and the northern spiral arm coincide spatially in some channels (given the geometry, they inevitably intersect), their kinematics are distinct from each other. The far W cloud moves almost directly westward (along the horizontal rectangle). There is emission from the northern spiral arm to the southwest of the horizontal rectangle, but this emission does not appear to move westward as is the case with the western cloud. Rather, the northern arm emission again remains in the same spatial location in each progressive channel. We emphasize that these effects are subtle, especially in the far W cloud. In the case of the far W cloud, additional observations at either higher resolution or more CO transitions are necessary to confirm whether it is indeed part of the outflow.

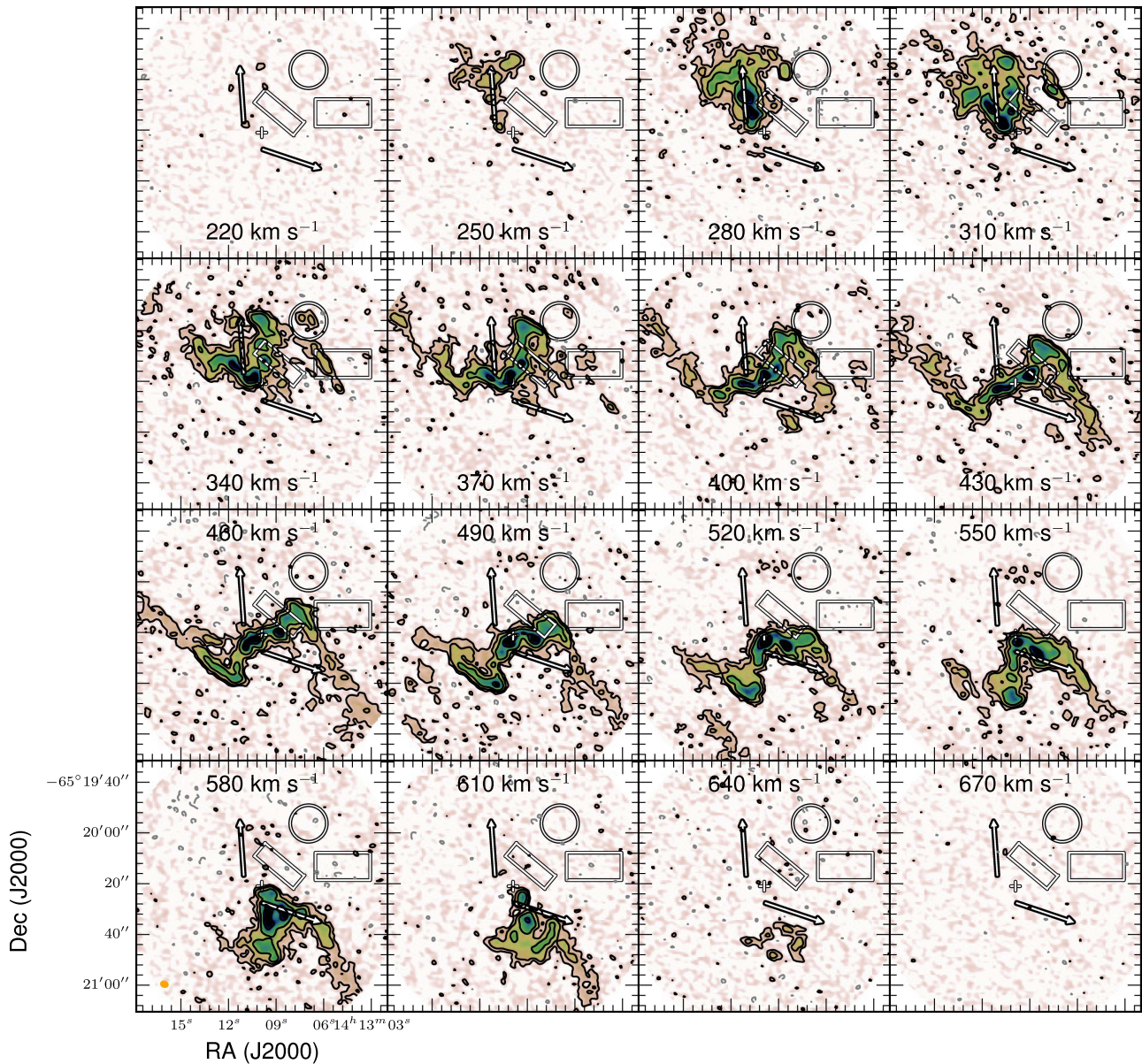


Figure 3. Channel maps of the CO (1–0) at 3 km s^{-1} showing every tenth channel. Contours begin at 3σ and increase by factors of three. Negative 3σ contours are shown in gray. Marked features are as in Figure 1. The beam is shown as the orange ellipse in the lower left corner. Note how there exists a large amount of spiral arm material at and near the systemic velocity (434 km s^{-1}), indicating substantial streaming. A potential 3σ counter-rotating feature is seen to the north (adjacent to the region containing the NW cloud) from $480\text{--}590 \text{ km s}^{-1}$. Deeper observations or observations of additional CO transitions will be able to tell if this feature is real. The feature traverses toward the center and elongates in the panel corresponding to 590 km s^{-1} .

4. RESULTS

4.1. The Molecular Outflow in Circinus

Although we identify a region of higher density and increased velocity dispersion where a molecular outflow would be expected, the outflow cannot be easily separated from disk material. Based on the ionized outflow (Figure 6), it is clear that much of the outflow overlaps and shares similar velocities to those of the disk in projection. Even with the higher velocity resolution of ALMA (3 km s^{-1}) as opposed to MUSE (57 km s^{-1}), we find that the kinematics are still difficult to disentangle. Furthermore, the orientation of the bar is such that it imposes higher surface brightness and non-circular velocities near the base of the outflow. The result is that the bar and outflow are indistinguishable (putting bar-symmetry arguments aside for now). Finally, the outflow to the northwest intersects

two spiral arms—one within $\sim 7''$ and another at larger radii beyond the central region of the main disk. The innermost spiral arm and bar are both avoided by not including the central $7''.5$ in our calculations. The northern spiral arm covers a larger radial extent and shows velocities clearly distinct from the main disk. Thus, we also exclude this overlapping region from our calculations. With these exclusions, a limited region remains (white box in Figure 4). For our calculations, we assume that any anomalous or overdense gas in this restricted region is indeed part of the molecular outflow.

To isolate potential outflowing material, we use four approaches. The first approach involves integrating over regions in which outflowing material is expected based on the available multiwavelength data and then subtracting the flux from the main disk. The second approach involves mirroring the velocity field of each half along the major axis

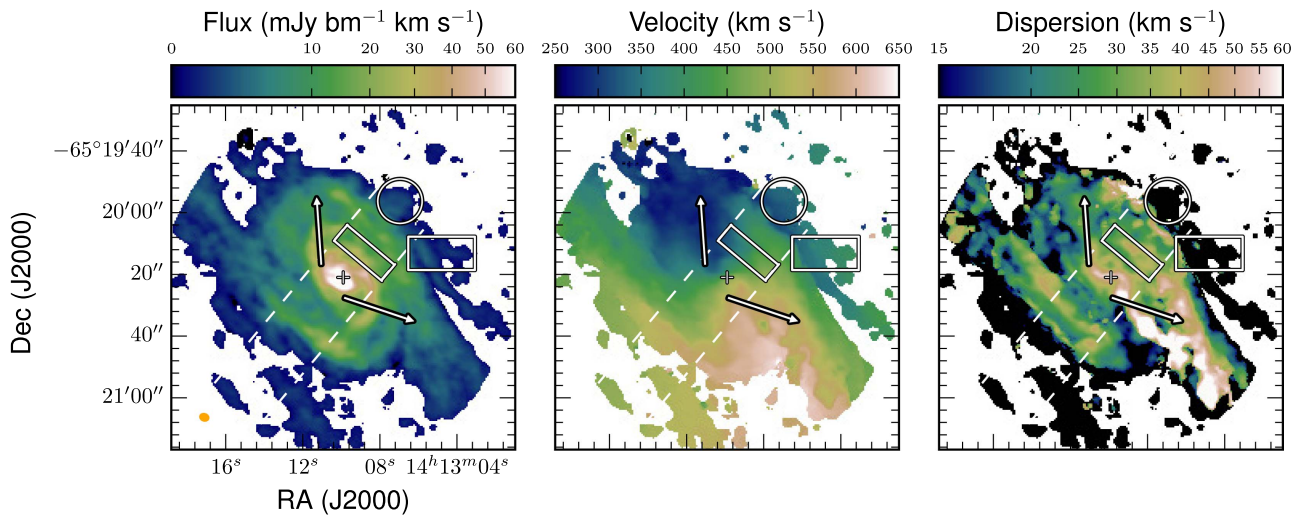


Figure 4. CO (1–0) moment maps of Circinus. Left: an integrated intensity (zeroth-moment) map of CO (1–0) in the central $\sim 1'$ of Circinus. Marked features are as in Figure 1 with the exception of the white dashed lines, which indicate the region considered in Figure 5. Note the overdensity in the northwest region extending $\sim 40''$ from the nucleus to the northwest. Center: the intensity-weighted velocity map (first-moment) of the same region. Overall, the disk displays normal rotation, with some disturbances to the southwest and northwest. Right: an intensity-weighted velocity dispersion (second-moment) map. Further north there is an abrupt ridge, possibly due to disk and/or outflowing material meeting the northern spiral arm, which has a different inclination from the rest of the disk. In all cases, the cube is masked at $13.5 \text{ mJy } \text{bm}^{-1}$ ($\sim 2.5\sigma$) prior to creating the maps. The beam is shown in orange in the bottom corner of the left panel.

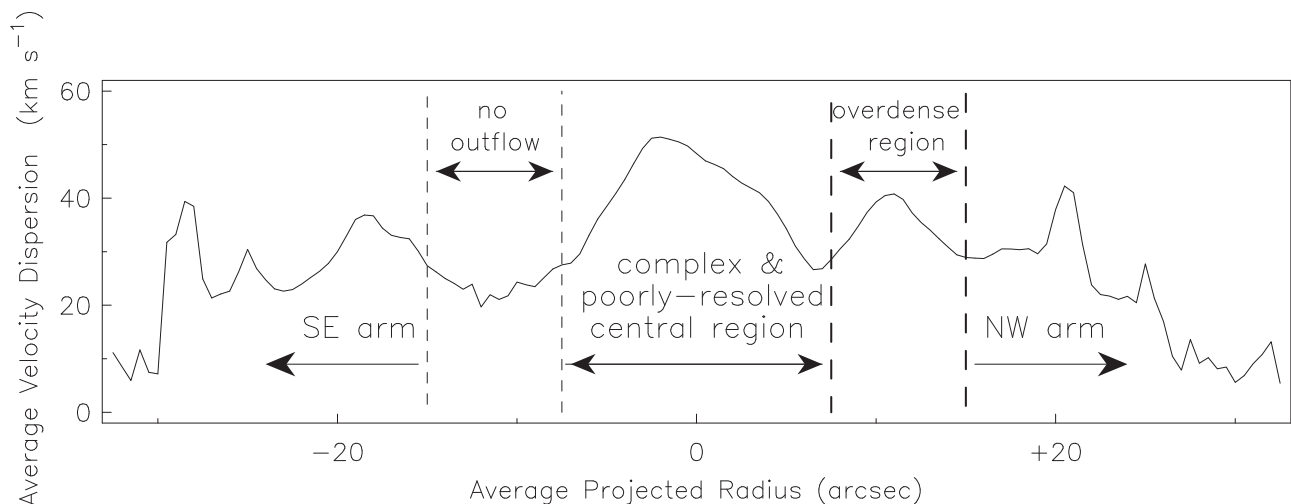


Figure 5. Average velocity dispersion with projected radius for a $20''$ wide strip along the region containing the outflow (white dashed lines in Figure 4). The central $\sim 7''.5$ are poorly resolved and contain a bar as well as spiral structure. Thus, they are not included in our estimates of the outflow properties. The NW and SW arm regions are also excluded. Considering only the remaining regions, there is a clear increase of a factor of approximately two in velocity dispersion over the $7.5 \times 20''$ “outflow” region containing the overdensity seen in Figure 4 as compared to the “no outflow” region 180° to the southeast (which itself has a velocity dispersion typical of a spiral disk).

and then subtracting them from each other in order to obtain a residual (e.g., Ho et al. 2016 for ionized outflows). A third method involves creating kinematic models of the main disk and then subtracting them from the data in order to isolate the wind that remains in the residuals (e.g., García-Burillo et al. 2014; Pereira-Santaella et al. 2016). The fourth approach considers a spectral analysis of select regions containing potential outflow features. The first two approaches are straightforward as presented in Sections 4.1.1 and 4.1.2, while the third approach is more involved, thus we present the results from that method in Section 4.1.3 and describe that process in the Appendix. The fourth method analyzes all potential outflow features that become evident via the first three methods, and is presented in Section 4.1.4.

4.1.1. The Molecular Outflow Based on Integrated Flux Measurements

We consider emission in the overdense region only from approximately $7''.5$ – $15''$ (330 – 650 pc deprojected). The region is enclosed by the white box in Figure 4. It is in between the spiral arms, which presents the possibility that some of the emission is from the spiral arms. However, for this calculation, we assume that all emission in excess of the disk is due to an outflow. To obtain this excess emission, we integrate the flux in the overdense region and do the same for the region of the disk to the southeast that is azimuthally opposite. We then subtract the latter from the former. The final value is the outflowing emission within the overdense region, which can then be converted into a luminosity in order to determine its molecular mass.

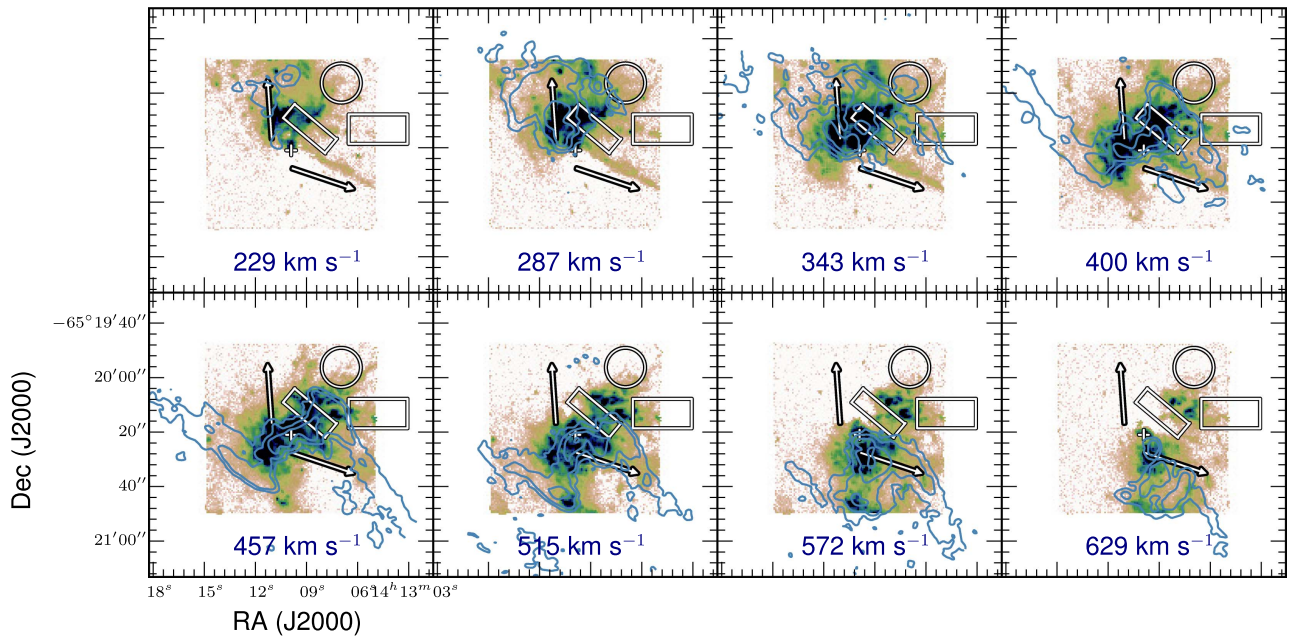


Figure 6. Channel maps showing the H α as observed with MUSE (for a more complete presentation of those data, see Marconi et al. 2016, in preparation, and Venturi et al. 2016, in preparation) with CO (1-0) moment maps spanning the corresponding MUSE velocities overplotted in blue. Contours begin at $7.5 \text{ mJy km}^{-1} \text{ km s}^{-1}$ and increase by factors of four. Marked features are as in Figure 1. While the ionized outflow is prominently seen in straight filaments directed primarily to the northwest, its velocities coincide with those of the main disk. The issue is compounded further for the molecular component as it also includes gas in the outer spiral arms. The outer arms do not follow disk rotation, thus rendering disentangling the molecular outflow from regions over which it intersects difficult.

4.1.2. Outflow Extraction via Inspection of Asymmetries in the Velocity Field

We employ a second method in which the velocity field is mirrored along the major axis and then subtracted in order to obtain a residual. This approach is similar to that taken by Ho et al. (2016) for ionized outflows in edge-on galaxies. While Circinus is moderately inclined, the same principles apply to first order. If a large difference is seen in the residuals outside of the effective radius of the molecular disk, and thus likely to be extraplanar, then it is an indicator of outflowing gas. While there are some differences as seen in Figure 8, the molecular gas is clearly not outflow-dominated. The greatest extremes are in the outermost spiral arms, but these are due to motions within the spiral arms themselves and not associated with a large-scale outflow.

4.1.3. Extracting the Outflow Through Kinematic Modeling

We utilize kinematic modeling as detailed in the Appendix to further separate the molecular outflow from the main disk, as well as the spiral arms, which presumably share the circular motions of the main disk. Residual moment maps are shown in Figure 9. The first set is after subtracting a simple disk model with no additional features. A second set of residuals is created by subtracting a simple disk, bar, and spiral arms (with radial motions).

The overdense region still contains substantial emission after the disk-only subtraction, while there is none remaining in the azimuthal range 180° to the southeast. The flux remaining in the overdense region has clearly distinct kinematics from the nearest remaining flux associated with the northern spiral arm. Curiously, this remaining emission in the overdense region has similar kinematics to those of the northwestern cloud, which is almost certain to be outflowing molecular gas. The remaining emission is also aligned in the same direction away from the disk as is the NW cloud.

Additional molecular gas is eliminated in the residuals created by subtracting models containing additional features. Much of the emission in the overdense region could alternatively be attributed to the spiral arm. However, the blueshifted feature remains and is still aligned with the NW cloud.

The far W cloud also remains in the final residuals, but it is clear that some of the gas on its eastern edge is indisputably associated with the northern spiral arm. However, this remaining gas from the arm is unsurprising given its presence in the panel corresponding to 340 km s^{-1} in Figure 3—the edges of the far W cloud and northern spiral arm simply overlap spatially, but at different velocities. It is demonstrated in the Appendix that not all of the northern spiral arm emission is eliminated in the residuals due to the difficulty in fully constraining the streaming motions within them.

Another feature, starting from the nucleus and extending almost directly north (along the northern arrow), becomes clear. This feature (henceforth referred to as the “northern stripe”) can also be seen in channel maps (Figures 3 and 7) extending from $340\text{--}460 \text{ km s}^{-1}$ in the former and all channels in the latter. In some regions along the extent of the northern stripe it is blueshifted as much as 110 km s^{-1} with respect to the peak (at the same pixel location), but blueshifted by approximately the same amount from systemic. The northern stripe is near the edge, but still within the extent of the wide-angled ionized outflow cone. The relatively extreme location of the northern stripe when compared to the central filaments renders it much simpler to disentangle than any other possible outflow components. Thus, a scenario in which only a single filamentary structure associated with the outflow near the edge of the cone is detected is possible.

Detailed descriptions of the models are given in the Appendix.

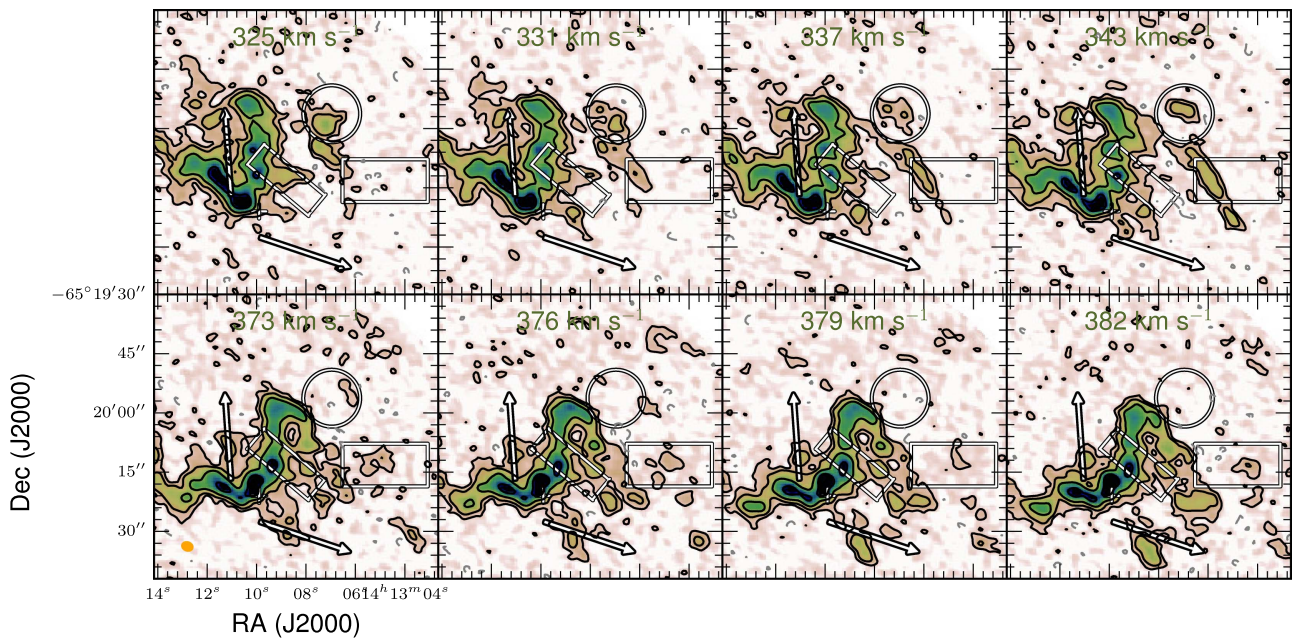


Figure 7. Channel maps showing the NW cloud (top row) and the far W cloud (bottom row). Contours are as in Figure 3 and marked features are as in Figure 1. The NW cloud moves in a northwest direction with velocity while the far W cloud moves in a western direction.

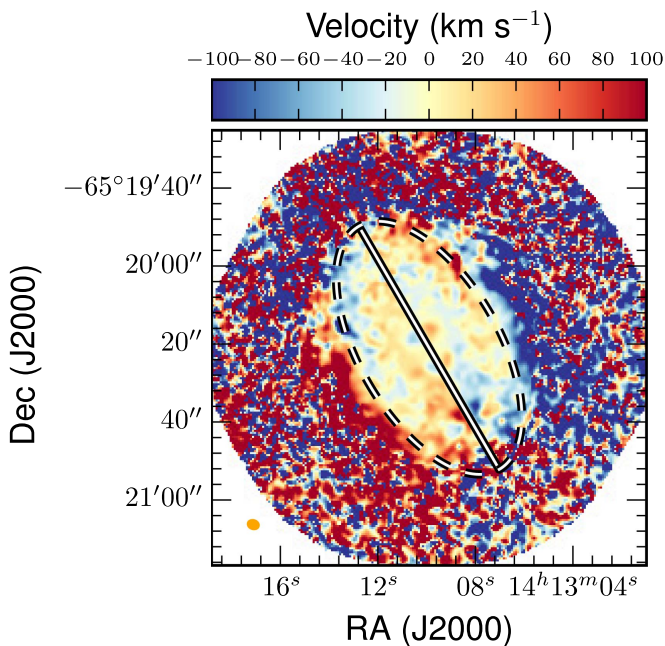


Figure 8. Residual resulting from subtracting the southeastern velocity field from the northwestern velocity field mirrored across the major axis. The line in the center is directly along the major axis, while the ellipse represents the radius of the projected molecular disk (not including the outermost spiral arms). The beam is shown in the lower left corner. If the disk were outflow-dominated, there would be a substantial difference in the two halves (appearing as red and blue extremes in color). The most extreme velocity differences are in the outermost spiral arms just beyond the ellipse. These extremes are due to motions within the spiral arms rather than related to an outflow from the nuclear regions.

4.1.4. A Spectral Analysis of the Outflow

Now that all anomalous features have been identified, we present representative spectra of these regions in Figure 10, with the spectra locations shown in Figure 11. The spectra in the overdense region consistently show blueshifted wings. The

northern stripe is blueshifted from systemic, but redshifted with respect to the approaching half of the galaxy. The former velocity shift is relevant when considering the outflow. The southern disturbance is again clearly seen as blueshifted from systemic. The NW and far W clouds are both blueshifted ($\sim 100 \text{ km s}^{-1}$ for the former and $40\text{--}50 \text{ km s}^{-1}$ for the latter).

Average spectra of the overdense region and azimuthally opposite region are shown in Figure 12. The blueshifted wing remains in the average spectrum for the overdense region, but there are no indications of a similar blueshifted feature in the region that is azimuthally opposite. There are, however, slight indications of a redshifted wing.

4.1.5. Molecular Outflow Parameters Determined from the Data

The first method considers the excess flux present in the overdense region when compared to the azimuthally opposite region to the southeast. This method provides a basic estimate for the mass of outflowing molecular gas. The second method provides no quantifiable results, but is rather a confirmation that Circinus is not outflow-dominated. The third method can, in theory, yield a mass estimate for the outflow, but not all of the emission can be disentangled from the main disk due to the shared rotation of the disk and outflow. All but $\sim 25\%$ of the potential outflowing material associated with the overdense region (first method) is eliminated by a disk-only subtraction, and all but a few percent is eliminated by our final model, which includes a bar and spiral arms (features with kinematic properties that cannot be unambiguously constrained). Because of the shared outflow/disk rotation that is known to exist in the ionized component, it is obvious that most of the potential outflowing molecular gas will be subtracted by this method and such a result should not be considered valid. Ultimately, a reliable outflow mass cannot be derived from this method in the case of Circinus. While the fourth method reinforces evidence for a molecular outflow, the spectra do not provide an improved means for determining the molecular mass itself. However, the fourth method provides clearer velocity measurements for the

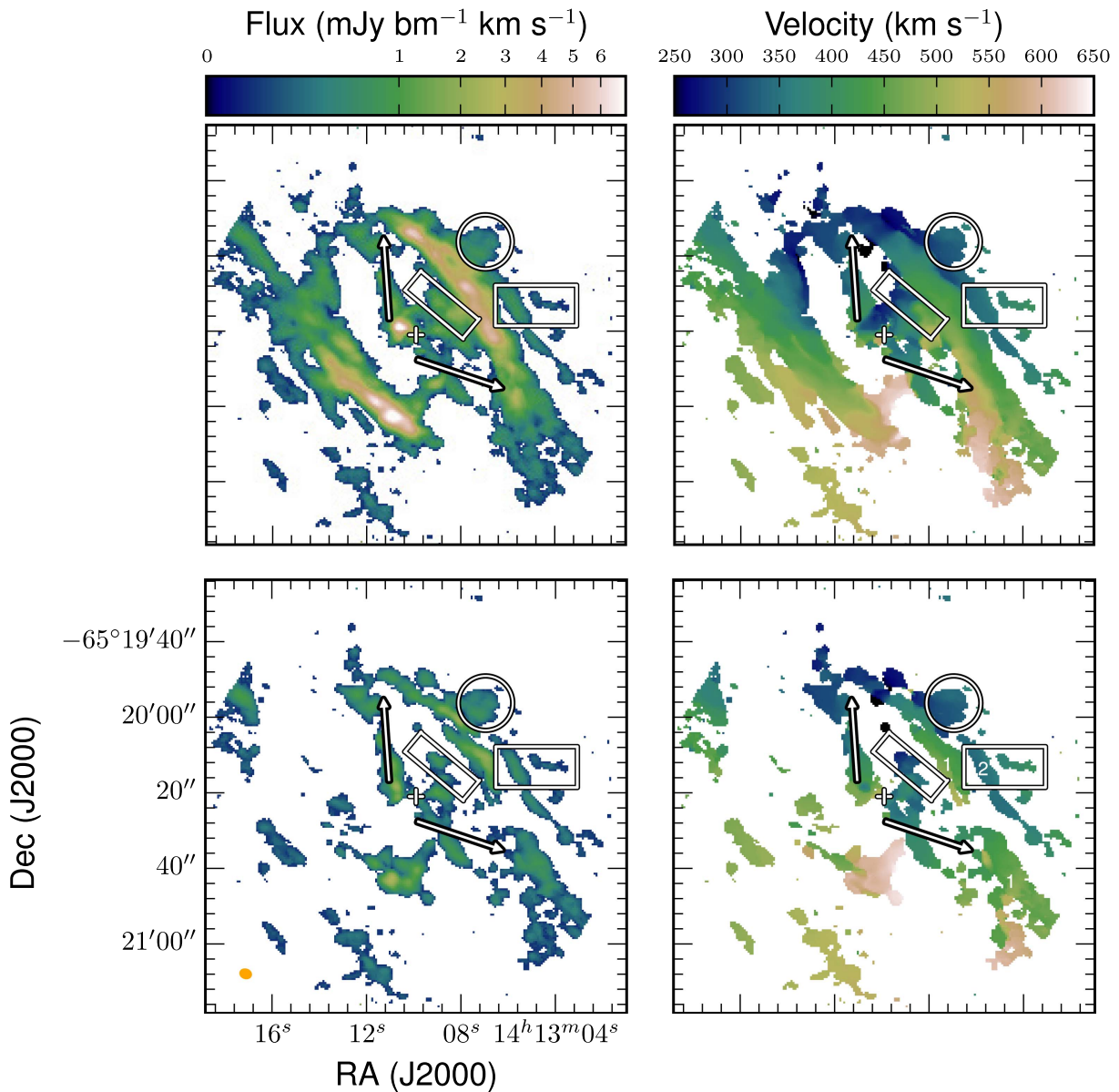


Figure 9. Zeroth- (left) and first- (right) moment maps created from two residuals clipped with a 30 mJy bm^{-1} threshold for clarity. The residuals after subtracting a simple disk model with no additional features are shown in the top row and residuals after subtracting a simple disk, bar, and spiral arms (with radial motions) are shown in the bottom row. Outlined regions are as in Figure 1. The beam is shown in the lower left corner in orange. The overdense region still contains substantial emission after the disk-only subtraction. The remaining flux in the overdense region after subtracting the final models (bottom, right panel) has clearly distinct kinematics (blueshifted $\sim 150 \text{ km s}^{-1}$) from the nearest remaining flux associated with the northern spiral arm in the same panel (denoted by “1”). This remaining emission in the overdense region has similar kinematics to the northwestern cloud—an almost certain outflow feature. Kinematically distinct sections of the spiral arms remaining after the final models are denoted by “1” and “2” to emphasize the distinction. The blueshifted emission directly south of the overdense region corresponds to the increased velocity dispersion to the south first introduced in Figure 4.

potential outflowing components. For these reasons, we use the numerical values derived using the first method for the mass-related quantities, and velocities derived from the fourth method (or optical in the case of the overdense region and upper limits) in the following calculations.

The CO luminosity associated with the outflow in the overdense region is $3.8 \times 10^6 \text{ K km s}^{-1} \text{ pc}^2$. Using the α_{CO} conversion factor of $0.34 M_{\odot} \text{ pc}^{-2} (\text{K km s}^{-1})^{-1}$ put forth in Bolatto et al. (2013b) for the lower limit of outflows, we obtain a molecular mass of $1.6 \times 10^6 M_{\odot}$, which is on the order of 0.3%–0.5% of the total molecular mass of the disk out to 2.6 kpc. Another reason to consider this α_{CO} value a lower limit is that Leroy et al. (2015b) find that their observed low-J

CO line ratios are difficult to reproduce in the optically thin case in the outflow of M82, thus indicating that it is not necessarily a valid assumption for the outflowing emission.

In addition to the overdense region, we include the NW and far W clouds as well as the northern stripe in our calculations. The southern disturbance is not included as it shows strong indications of being associated with the northern spiral arm, especially when considering its furthest extent to the southwest.

We determine the CO luminosity of the NW cloud as $6.2 \times 10^5 \text{ K km s}^{-1} \text{ pc}^2$ and its molecular mass to be $2.1 \times 10^5 M_{\odot}$ using $\alpha_{\text{CO}} = 0.34 M_{\odot} \text{ pc}^{-2} (\text{K km s}^{-1})^{-1}$. The values for the far W cloud under the same assumptions are $9.2 \times 10^4 \text{ K km s}^{-1} \text{ pc}^2$ and $3.1 \times 10^4 M_{\odot}$. Finally, the

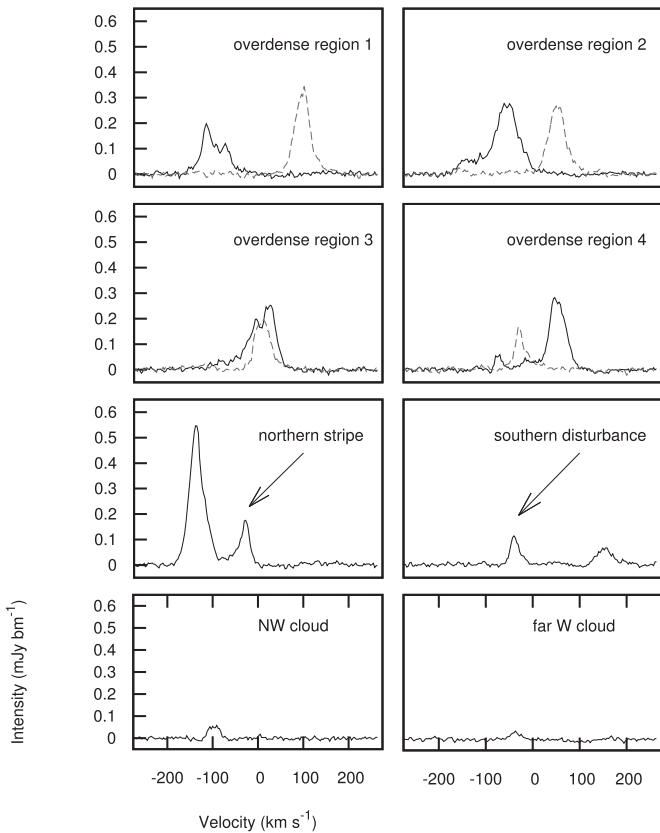


Figure 10. Representative spectra from regions containing molecular gas with anomalous velocities. Spectra locations are shown in Figure 11 and correspond to the features originally shown in Figure 1. The top four panels show spectra from the overdense region (black solid lines), with the corresponding spectra that are azimuthally opposite (gray dashed lines). With the exception of the top left panel (corresponding to the northernmost overdense region spectrum and the southernmost azimuthally opposite spectrum), all of the spectra in the overdense region have low-level blueshifted wings. Spectra in the azimuthally opposite region show hints of redshifted wings.

corresponding values for the northern stripe are $1.2 \times 10^6 \text{ K km s}^{-1} \text{ pc}^2$ and $4.2 \times 10^5 M_{\odot}$. The luminosities for the overdense region and far W cloud have no measured uncertainties as the boundaries for these features are clear. In the case of the overdense region, the box is clearly defined. The measurement of the far W cloud does not include any ambiguous diffuse emission or overlap with any other structures. The NW cloud and the northern stripe, however, have measured uncertainties in their CO luminosities due to their proximity to larger-scale structures. These uncertainties are on the order of 30%.

We now determine the mass outflow rate. As was also done in Bolatto et al. (2013a) for the case of NGC 253, we use the following formula based on the morphology of the outflow:

$$\dot{M} = \frac{2\alpha_{\text{CO}} L_{\text{CO}} v_w \tan i}{r_w} \quad (1)$$

where L_{CO} is the CO luminosity (already multiplied by α_{CO} , the conversion factor discussed in the last section), v_w is the projected velocity of the outflow, i is the inclination of the outflow, and r_w is the extent of the outflow in projection. For an initial estimate, we assume $v_w = 150 \text{ km s}^{-1}$ based on the highest velocities we see in the molecular component and the optical velocities (180 km s^{-1}) as seen in Veilleux & Bland-

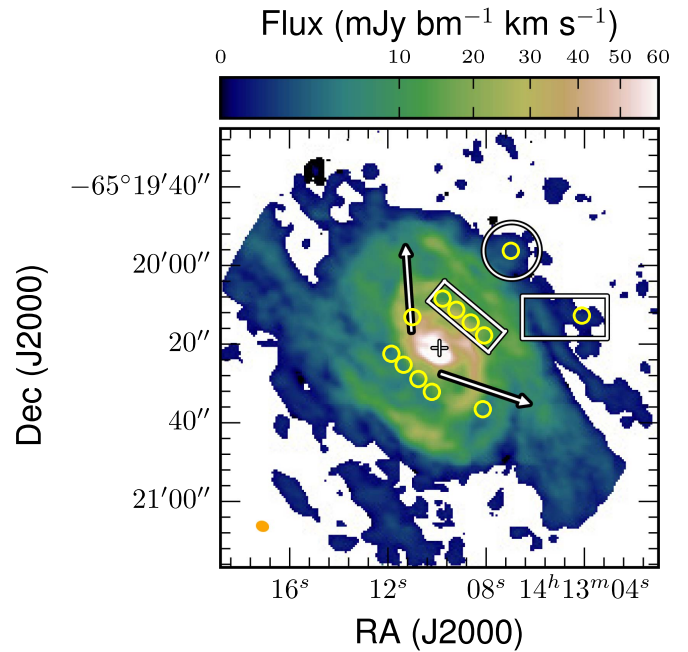


Figure 11. A zeroth-moment map showing the locations of spectra in Figure 10. The spectra are single pixels at the center of each yellow circle. The northernmost circle in the overdense region represents “overdense region 1” in Figure 10, going in order to “overdense region 4” to the southwest. Spectra in the azimuthally opposite region are in reverse order, starting from the southernmost (“region 1”) and going to the northeast.

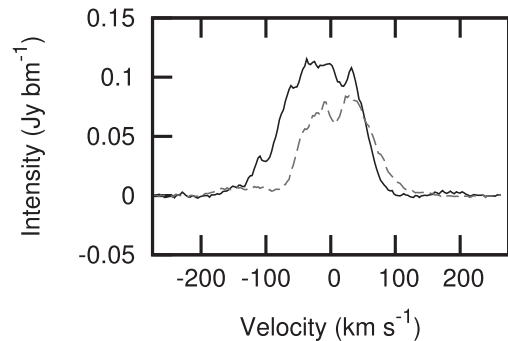


Figure 12. Average spectrum over the overdense region (black solid line) and the region azimuthally opposite (gray dashed line).

Hawthorn (1997). Based on the NW cloud, the outflow is estimated to extend $\sim 35''$ (700 pc in projection, 1.5 kpc deprojected). However, the overdense region over which we integrate only extends from $7''.5$ (150 pc in projection, 0.3 kpc deprojected) to $22''.5$ (450 pc in projection, 1.0 kpc deprojected). Thus, for calculating the outflow rate of gas associated with the overdense region, we assume this range. While the outflow cone must have some range of inclinations with respect to the observer, for simplicity we assume it is perpendicular to the disk inclination of 65° . Based on these assumptions, we determine a molecular mass outflow rate of $3.0 M_{\odot} \text{ yr}^{-1}$ in the overdense region. While we use lower limit assumptions for this calculation, this value should not be considered a lower limit in the strictest sense as there may be material included in our mass estimate that is actually part of the spiral arms. Rather, it is a lower limit provided that the excess flux in the overdense region is indeed due to outflowing material.

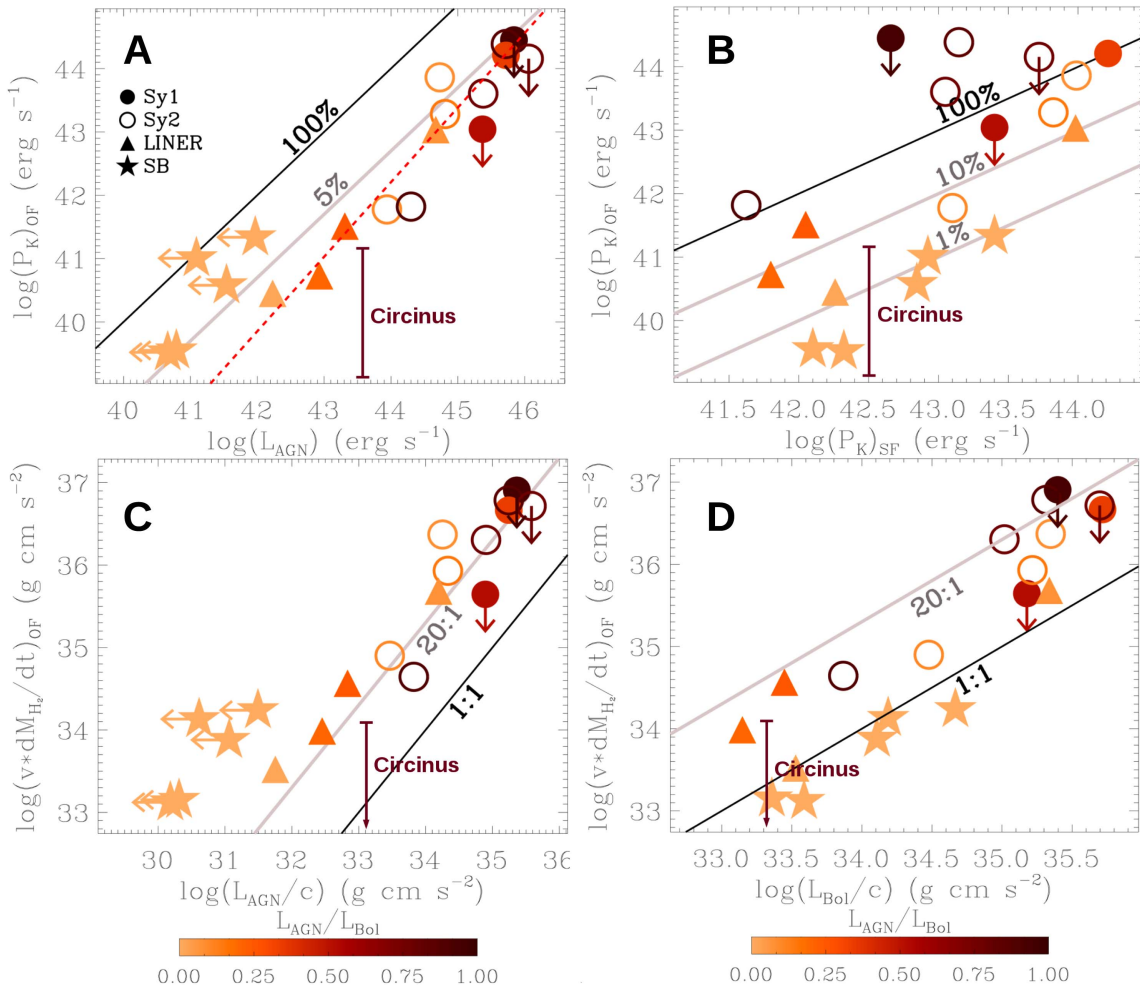


Figure 13. Figures 12 (panel (A)), 13 (panel (B)), 14 (panel (C)), and 16 (panel (D)) reproduced directly from Ciccone et al. (2014) (with permission), but with the addition of Circinus here. Symbols labeled in panel (A) correspond to Seyfert 1 (Sy1), Seyfert 2 (Sy2), LINER, and starburst (SB) galaxies. The ranges for $P_{\text{kin,OF}}$ and $v\dot{M}_{\text{H}_2,\text{OF}}$ for Circinus have been added where applicable. It is important to note that $\alpha_{\text{CO}} = 0.8$ was assumed for the galaxies in the Ciccone et al. (2014) work (upper end of range shown for Circinus). In all cases, $P_{\text{kin,OF}}$ and $v\dot{M}_{\text{H}_2,\text{OF}}$ for Circinus is significantly lower than that of the AGN-driven outflows, especially those with high $L_{\text{AGN}}/L_{\text{BoI}}$. However, when considering the upper limit of $\alpha_{\text{CO}} = 0.8$ (typically used for ULIRGs) in the case of Circinus, it appears to follow the relation indicated by the Seyfert 2 galaxies when extrapolated to lower L_{AGN} .

To derive an upper limit for the overdense region, we assume a maximum velocity of 180 km s^{-1} as in Veilleux & Bland-Hawthorn (1997). We also assume a higher α_{CO} of $0.8 M_{\odot} \text{ pc}^{-2} (\text{K km s}^{-1})^{-1}$ for an optically thick case. These assumptions yield a mass outflow rate of $8.3 M_{\odot} \text{ yr}^{-1}$ in the overdense region.

The NW cloud also contributes to the molecular mass outflow rate. Assuming the cloud extends from roughly $25''$ – $35''$ (510 – 700 pc in projection, 1.1 – 1.5 kpc deprojected) with a velocity of 100 km s^{-1} and α_{CO} of 0.34 , we obtain a lower limit of $0.35 M_{\odot} \text{ yr}^{-1}$. In contrast to the value calculated for the overdense region, *this is a strict lower limit* because the NW cloud appears to be outflowing from the galaxy. Assuming 180 km s^{-1} (on the higher end of the optical velocities) and α_{CO} of 0.8 , an upper limit for the molecular mass outflow rate of the NW cloud is $2.5 M_{\odot} \text{ yr}^{-1}$. These values also consider the $\sim 30\%$ uncertainty in the CO luminosity measurement.

The far W cloud contributes a negligible amount to the molecular mass outflow rate. We use the same approximations as for the NW cloud, with the exception of the velocity, which we assume to be 50 km s^{-1} , and obtain a lower limit of $0.03 M_{\odot} \text{ yr}^{-1}$ and an upper limit of $0.08 M_{\odot} \text{ yr}^{-1}$.

Also assuming 50 km s^{-1} , but a total radial extent of $20''$, we find the molecular mass outflow rate associated with the northern stripe is 0.2 – $0.7 M_{\odot} \text{ yr}^{-1}$. These values also consider the $\sim 30\%$ uncertainty in the CO luminosity measurement.

If one includes the overdense region, clouds, and northern stripe in the total, the molecular mass outflow rate is 3.6 – $12.3 M_{\odot} \text{ yr}^{-1}$. We again emphasize that the lower limit assumes that all excess flux in the overdense region is due to outflowing molecular gas. The strictest lower limit is $0.35 M_{\odot} \text{ yr}^{-1}$, which only includes the outflowing NW cloud.

For et al. (2012) list a range of possible global SFRs for Circinus, derived by different authors using a variety of methods. We adopt the value of $4.7 M_{\odot} \text{ yr}^{-1}$ calculated by Zhu et al. (2008) using the total infrared luminosity (L_{TIR}). The molecular mass outflow rate of 0.35 – $12.3 M_{\odot} \text{ yr}^{-1}$ is a comparable to the global SFR in Circinus and thus may significantly affect SF in its central regions.

We find the molecular mass of the observed disk (out to $\sim 1.5 \text{ kpc}$) to be $2.9 \times 10^8 \pm 8.7 \times 10^7 M_{\odot}$ assuming an α_{CO} of $4.3 M_{\odot} \text{ pc}^{-2} (\text{K km s}^{-1})^{-1}$ from Bolatto et al. (2013b). This α_{CO} has an uncertainty of $\sim 30\%$ and is based on typical values for the Milky Way disk that are derived using a variety of

methods including CO isotopologues and dust extinction. This molecular disk mass indicates that if the gas were actually leaving the galaxy with a constant mass outflow rate of $0.35\text{--}12.3 M_{\odot} \text{ yr}^{-1}$, the molecular gas would be depleted on the order of $10^7\text{--}10^8$ year. Although, with the outflow velocity being substantially less than the escape velocity, the molecular gas will most likely be reaccreted. This conclusion is based on the peak rotational velocity of $\sim 200 \text{ km s}^{-1}$ (derived in the Appendix), which yields an escape velocity $\geq 500 \text{ km s}^{-1}$ near the center (Binney & Tremaine 2008). Alternatively, Martin (2005) provides an estimate of the escape speed of a few times the rotational velocity from the halo. The projected velocity of the outflow does not come close to reaching either estimate (although we cannot be certain about velocities across the line of sight).

The kinetic power ($P_{\text{kin,OF}} = \frac{1}{2}v^2\dot{M}_{\text{H}_2,\text{OF}}$) and momentum rate ($v\dot{M}_{\text{H}_2,\text{OF}}$) of the molecular outflow can also be estimated from these data. Using the lower and upper limits for the mass outflow rates determined above, we find a range of $1.0 \times 10^{39}\text{--}1.1 \times 10^{41} \text{ erg s}^{-1}$ for the $P_{\text{kin,OF}}$, and $2.0 \times 10^{32}\text{--}1.3 \times 10^{34} \text{ g cm s}^{-2}$ for ($v\dot{M}_{\text{H}_2,\text{OF}}$).

4.2. Additional Detected Lines

In addition to CO(1–0), we detect two groups of CN (1–0) radicals—four hyperfine $J = 1/2$ transitions at ~ 113.15 GHz, and five $J = 3/2$ hyperfine transitions at ~ 113.5 GHz. While the fine structure of the lines is difficult to disentangle, the rest frequencies of each transition are 113.191–113.123 GHz in the former group and 113.488–113.520 GHz in the latter. CN is a photodissociation region (PDR) tracer (e.g., Tielens & Hollenbach 1985), which is consistent with it being heavily concentrated at the nucleus as we see in Circinus.

C^{17}O is also detected in Circinus—one of very few extragalactic detections to date (e.g., NGC 253, M82, and IC 342 by Sage et al. 1991; M51 by Watanabe et al. 2014). C^{17}O is a secondary nucleosynthesis product of low/intermediate mass SF. The current data do not provide detailed maps of its distribution. However, as suggested by Sage et al. (1991), by mapping its distribution, deeper and higher resolution observations will yield insight concerning where different mass SF is taking place (e.g., when compared with CO (1–0), a high ratio of C^{17}O indicates low/intermediate SF, whereas a low ratio indicates massive SF).

5. DISCUSSION

5.1. Energetics of the Outflow

We now consider how the AGN and SF in Circinus may be affecting the outflow properties.

Circinus hosts a $10^{10} L_{\odot}$ AGN (Moorwood et al. 1996) and has a bolometric luminosity (L_{bol}) of $1.7 \times 10^{10} L_{\odot}$ (Siebenmorgen et al. 1997; Maiolino et al. 1998). These values yield $L_{\text{AGN}}/L_{\text{bol}}$ of around 0.6 (closer to 0.9 if using values derived in Stone et al. 2016). L_{AGN} for Circinus is comparable to that of NGC 1266, NGC 1068, and NGC 1377 (Cicone et al. 2014 and references therein), and thus on the lower end of AGN luminosities for the molecular outflows observed to date. $L_{\text{AGN}}/L_{\text{bol}}$ for Circinus, however, is 2–3 times higher than for those galaxies.

Relevant to the launching mechanism of the outflow are its kinetic power and momentum rate. Observations show that

these properties, when associated with AGN-driven outflows, show some correlation with L_{AGN} (e.g., Cicone et al. 2014; Feruglio et al. 2015). Such connections have also resulted from simulations (e.g., Faucher-Giguère & Quataert 2012; Zubovas & King 2012).

The kinetic power of $1.0 \times 10^{39}\text{--}1.1 \times 10^{41} \text{ erg s}^{-1}$ which we determine for the molecular outflow is generally lower than that of the Cicone et al. (2014) sample, especially the outflows assumed to be driven by AGNs. In that work, a relation was established between the kinetic power of the outflows and the L_{AGN} of the host galaxies (generally finding that the $P_{\text{kin,OF}}$ is $\sim 5\%$ of L_{AGN}). Circinus has a substantially lower $P_{\text{kin,OF}}/L_{\text{AGN}}$ ratio (on the order of 0.01%–0.3% of L_{AGN}) compared to the ULIRGs and other Seyferts. However, this range is consistent with the linear fit expressed in Equation (3)/Figure 12 of Cicone et al. (2014). We directly duplicate Figure 12 from that work here with the addition of Circinus (Figure 13, panel (A)). In that relation, $P_{\text{kin,OF}}/L_{\text{AGN}}$ decreases for lower L_{AGN} , indicating that the trends derived from that sample may indeed apply to lower luminosity galaxies as well. The relation does not, however, appear to be consistent with the high ratio of L_{AGN} to L_{bol} in Circinus.

The kinetic power due to supernovae ($P_{\text{kin,SF}}$) is also useful to consider. Equation (2) from Veilleux et al. (2005) indicates that $P_{\text{kin,SF}} = 7 \times 10^{41} \text{ SFR}(M_{\odot} \text{ yr}^{-1})$, yielding a value of $3.5 \times 10^{42} \text{ erg s}^{-1}$ for Circinus—again low given its AGN properties. When $P_{\text{kin,OF}}$ is plotted against $P_{\text{kin,SF}}$, $P_{\text{kin,OF}}$ for Circinus is well below that of the AGN-driven outflows with $L_{\text{AGN}}/L_{\text{bol}}$ summarized in Figure 13 of Cicone et al. (2014), which we show here in panel (B) of Figure 13. Instead, Circinus falls within the LINER and starburst population.

We find the momentum rate of the molecular outflow is $2.0 \times 10^{32}\text{--}1.3 \times 10^{34} \text{ g cm s}^{-2}$. With these values, we find a ratio of $v\dot{M}_{\text{H}_2,\text{OF}}$ to L_{AGN}/c of 0.1–10.3. Cicone et al. (2014) found this ratio to be ~ 20 (and often significantly higher) for outflows in host galaxies having $L_{\text{AGN}} \geq 10\%$ of L_{bol} . The ratio found in that work is consistent with simulations presented by Zubovas & King (2012). Circinus is well below this ratio, again indicating that it does not have similar outflow properties to other galaxies with high values of $L_{\text{AGN}}/L_{\text{bol}}$. However, if one considers only the ratio of $v\dot{M}_{\text{H}_2,\text{OF}}/L_{\text{AGN}}$, the upper limit for Circinus derived using $\alpha_{\text{CO}} = 0.8$ (typically used for ULIRGs) is again consistent with the Cicone et al. (2014) trend seen in the galaxies with presumed AGN-driven outflows if one extrapolates to lower L_{AGN} (Figure 14 of Cicone et al. 2014 or panel (C) of Figure 13 here). When $v\dot{M}_{\text{H}_2,\text{OF}}$ is considered only in relation to L_{bol} , Circinus again appears to be consistent with starburst galaxies and LINERS (Figure 16 of Cicone et al. 2014 or panel (D) of Figure 13 shown here).

In summary, when considering the kinetic power and momentum rate, Circinus appears to be consistent with trends put forth in Cicone et al. (2014), with the exception of those connected to its high AGN luminosity (and $L_{\text{AGN}}/L_{\text{bol}}$).

5.2. The Multiphase Structure of the Wind

While there is a clear ionized outflow in Circinus, the existence of one in the molecular phase is ambiguous. In the preceding sections we have presented the strongest evidence for one within the ALMA data. (1) There is an overdensity to the northwest of the nucleus. This overdense region coincides with the location of the ionized outflow cone. (2) There is a

cloud to the northwest (NW cloud) that appears to be traveling away from the disk. The NW cloud is also blueshifted by approximately the same amount as the ionized outflow. This feature is the clearest outflow signature in the ALMA data. Based on the NW cloud, the molecular outflow is driven $\sim 35''$ in projection from the center, or 1.5 kpc when deprojected. (3) A similar but less prominent cloud is seen to the west (far W cloud). The far W cloud is directly along one of the ionized filaments, with velocities that coincide with that filament.

The ionized outflow to the northwest in Circinus is well-known, manifesting as a ~ 1.5 kpc blueshifted outflow cone (e.g., Marconi et al. 1994; Veilleux & Bland-Hawthorn 1997; Wilson et al. 2000; Sharp & Bland-Hawthorn 2010). All of these studies have noted the wide opening angle of the outflow cone, as well as filamentary structures. Veilleux & Bland-Hawthorn (1997) note the presence of bow-shocked features, indicating strong interactions with the ISM. Sharp & Bland-Hawthorn (2010) found evidence for a filled ionized gas cone and velocity gradients along filaments. The current resolution of the molecular data does not allow for a direct comparison with the ionized outflow, but the features that we see have similar velocities. Like the ionized component, it is possible that unidentifiable molecular outflow material exists that is kinematically indistinct from disk emission.

While we detect outflow signatures only on the near-side of the galaxy (also consistent with ionized observations), a counter-jet indeed exists, as shown by Elmouttie et al. (1998), in the radio continuum. If the aforementioned overdense region is truly due to a molecular outflow, the lack of a molecular component to the counter-jet is somewhat intriguing as it was previously thought that the lack of a symmetric ionized component was due to absorption. The counter-jet presented in Elmouttie et al. (1998), however, shows a substantial gap ($\sim 2'$ or 5–6 kpc, taking projection effects into account) between the main disk and the radio emission on that side, indicating that perhaps any molecular component is either weaker on that side or no longer present. There is also the possibility of asymmetries in the disk that could hinder the expulsion of material on one side.

Interestingly, Stone et al. (2016) searched for OH outflows in more than 50 low-luminosity Burst-Alert-Telescope-detected AGNs, including Circinus. In the case of Circinus, they found an unambiguous OH *inflow* in the form of an inverted P-Cygni profile within the innermost $\sim 10''$ from the center. Most of this region is omitted from our analysis due to resolution limitations. Thus, a valid comparison must wait for higher-resolution data.

5.3. Implications for the Evolution of Circinus

As demonstrated, it is difficult to detect outflowing molecular gas in Circinus. The kinematics of the disk and any potential outflow are largely overlapping for the ionized outflow, as demonstrated in Figure 6. We see multiple indications of a molecular outflow in the ALMA data, including the overdense region, the NW cloud and far W clouds, and the northern stripe. Still, there is no indication in the molecular phase of a prominent outflow such as what is seen in the ionized component (which is clearly seen even without kinematic information). Furthermore, even when we consider all potential outflowing molecular gas, its mass, mass outflow rate, and energetics are substantially lower than what are seen in AGN-driven outflows (Cicone et al. 2014),

especially when considering its high $L_{\text{AGN}}/L_{\text{bol}}$ ratio. We now consider possible explanations for this result.

Circinus has one of the most highly ionized narrow-line regions, which is visible in the optical, near-infrared, and mid-infrared (e.g., Contini et al. 1998; Prieto et al. 2010). Veilleux & Bland-Hawthorn (1997) find evidence that the higher resolution ionized component is launched from the region containing the AGN. The ionized component of the outflow from the central regions of Circinus is prominent (e.g., Marconi et al. 1994; Veilleux & Bland-Hawthorn 1997; Sharp & Bland-Hawthorn 2010). Thus, it is likely that a majority of the gas in the outflow cone of Circinus is in the ionized phase, resulting in a weak detection of outflowing CO.

It is difficult to say whether the molecular component of the outflow is entrained gas, or if the ionized component condenses and forms molecular gas in situ. Higher-resolution observations (especially on a level comparable to that of the MUSE data) and additional CO transitions, as well as shock tracers, will help to answer this question.

6. SUMMARY

(1) We observe the central $\sim 1'$ of Circinus galaxy with ALMA, targeting the CO(1–0) emission line, also detecting CN (1–0) ($J = 3/2-1/2$ and $F = 3/2-1/2$) and C^{17}O .

(2) The molecular disk exhibits primarily circular rotation and shows indications of a bar out to $\sim 10''$ (220 pc) as well as spiral arms. The spiral arms exhibit mild asymmetries and extend beyond the rest of the molecular disk in radius. The spiral arms also appear to have prominent (over 100 km s^{-1}) streaming motions.

(3) An overdensity of molecular gas exists to the northwest of the center of the galaxy that does not appear to be associated with the spiral arms (although it likely intersects them, especially at larger radii). The overdense region also has a higher average velocity dispersion than the rest of the disk and shows indications of non-circular motions. The gas in this region appears to be blueshifted compared to the main disk, consistent with the velocities of the ionized outflow. Most of the anomalous gas in this region is, however, faint compared to the rest of the disk, indicative of a diffuse outflow.

(4) Based on residuals after removing gas having circular motions, we see some indication of filamentary structures entrained in the wind. These structures require higher resolution and multiphase data to confirm.

(5) The total molecular mass of the disk within ~ 1.5 kpc is $2.9 \times 10^8 \pm 8.7 \times 10^7 M_{\odot}$. With the same assumptions, the molecular mass of the outflow in the overdense region, NW and far W clouds, and northern stripe (all included) is $1.8 \times 10^6 - 5.1 \times 10^6 M_{\odot}$, resulting in a molecular outflow rate of $3.6 - 12.3 M_{\odot} \text{ yr}^{-1}$. The strictest lower limit for the molecular mass and molecular mass outflow rate, which only includes the northwestern cloud (an unambiguous outflow feature) are $1.5 \times 10^5 M_{\odot}$ and $0.35 M_{\odot} \text{ yr}^{-1}$, respectively. The values within these ranges are generally comparable to our adopted SFR of $4.7 M_{\odot} \text{ yr}^{-1}$. However, any outflowing material is likely reaccreted due to its low velocity compared to the escape velocity of Circinus.

(6) The molecular outflow rate is lower than for AGN-driven molecular outflows presented in the literature (e.g., Cicone et al. 2014). However, the existing literature sample is biased toward strong and massive outflows with the result for Circinus perhaps being more typical for most galaxies.

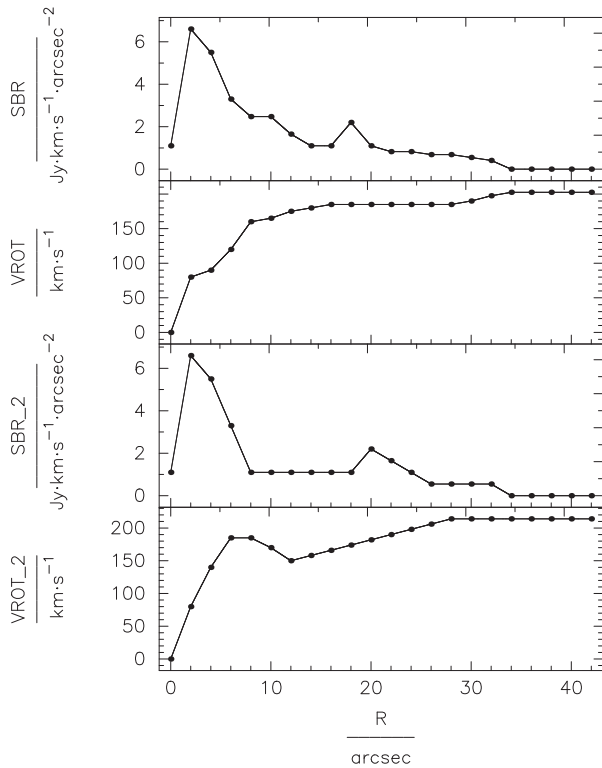


Figure 14. Rotation curves and surface brightness for the models prior to adding the bar and spiral arms as they cannot be quantified over all radii in the same manner. The approaching half is shown in the top panels, and the receding half is shown in the bottom.

(7) The kinetic power and momentum rate of the outflow are lower than those presented in Cicone et al. (2014) for AGN-driven molecular outflows (especially given its high L_{AGN} to L_{bol} ratio), although it fits the predictions of some linear relations presented in that work (e.g., $P_{\text{kin,OF}}$ versus L_{AGN}). When considering $v\dot{M}_{\text{H}_2,\text{OF}}$ compared to L_{bol} , Circinus is more consistent with the starburst galaxies within that sample.

First, we thank the referee for constructive comments and feedback that led to improvement of this manuscript, especially in its clarity. The National Radio Astronomy Observatory is a facility of the National Science Foundation operated under cooperative agreement by Associated Universities, Inc. This paper makes use of the following ALMA data: ADS/JAO.ALMA#2013.1.00247.S. ALMA is a partnership of ESO (representing its member states), NSF (USA), and NINS (Japan), together with NRC (Canada), NSC, and ASIAA (Taiwan), and KASI (Republic of Korea), in cooperation with the Republic of Chile. The Joint ALMA Observatory is operated by ESO, AUI/NRAO, and NAOJ. This research made use of APLpy, an open-source plotting package for Python hosted at <http://aplpy.github.com>. Based on observations made with the NASA/ESA *Hubble Space Telescope*, obtained [from the Data Archive] at the Space Telescope Science Institute, which is operated by the Association of Universities for Research in Astronomy, Inc., under NASA contract NAS 5-26555. These observations are associated with program #U4IM0101R. Based on data products from observations made with ESO Telescopes at the La Silla Paranal Observatory under programme ID 094.B-0321. J.M.D.K. gratefully acknowledges financial support in the form of a Gliese

Fellowship and an Emmy Noether Research Group from the Deutsche Forschungsgemeinschaft (DFG), grant number KR4801/1-1. E.P.F. acknowledges funding through the ERC grant “Cosmic Dawn.” We thank I-Ting Ho, Filippo Fraternali, and Kazimierz Sliwa for stimulating discussions concerning outflows and molecular chemistry. We thank C. Cicone for permission to reproduce figures originally published in Cicone et al. (2014). We thank A. Marconi for discussion concerning the status of work related to the MUSE data. We also thank R. G. Sharp for supplying optical IFU data of Circinus originally published in Sharp & Bland-Hawthorn (2010), which were helpful in our initial analysis but are not included here.

APPENDIX KINEMATIC MODELING OF THE MOLECULAR DISK

In an attempt to extract emission with non-circular motions, we create a model galaxy cube. We then subtract this model galaxy cube from the data cube in order to obtain residuals. This approach, however, is very limited in the case of Circinus. It is clear from recently observed IFU data of the ionized component (Figures 1 and 6) that the outflow velocities substantially overlap with those of the main disk. Further complicating this approach are the bar and spiral arms in Circinus, the former being aligned in the direction of the outflow and the latter intersecting it at least twice (both as seen in projection). With these issues in mind, a basic model galaxy is created in order to extract as much of the outflow as possible.

We employ tilted ring modeling (Rogstad et al. 1974) to characterize the properties of the main disk using the Tilted Ring Fitting code (TiRiFiC, Józsa et al. 2007). The model galaxy is comprised of a series of concentric rings for each of which we specify the surface brightness, inclination, position angle, rotational velocity, velocity dispersion, scale height, systemic velocity, and central position. Thus, features such as warps, flares, bars, and spiral arms can be modeled. Due to asymmetries, we model the approaching and receding halves of the galaxy separately. A more detailed description of the modeling process can be found in Zschaechner et al. (2012), Gentile et al. (2013), and Zschaechner & Rand (2015) among others.

Initial estimates for the surface brightness are based on the distribution along the major axis. The rotation curve is determined using the terminal side of the major axis position–velocity (lv) diagram (Figure 15). These parameters are continuously refined throughout the modeling process. The velocity dispersion is gauged by the spacing of the contours on the terminal sides of all position–velocity diagrams and is found to be 15 km s^{-1} for the main disk, but closer to 45 km s^{-1} in the central few arcseconds. (Recall that the higher dispersion at the center is likely due to the presence of a bar, thus it is not included in the models themselves.) Several values for the exponential scale height are tested throughout modeling, including scenarios in which the scale height varies radially (although such variations are deemed unnecessary for a good fit). A final value of $4''$ (80 pc in projection) is used. The inclination is initially assumed to be 65° . Additional values ranging from 50° to 70° are tested, but 65° is found to be the best fit throughout the disk. Position angles between 200° and 230° are tested, with an optimal value of 210° . Although, in the regions observed, the position angle is not best fit with a single value, but with fluctuations due to the bar and spiral arms (or a bar and spiral arms superimposed as we have done in our final model).

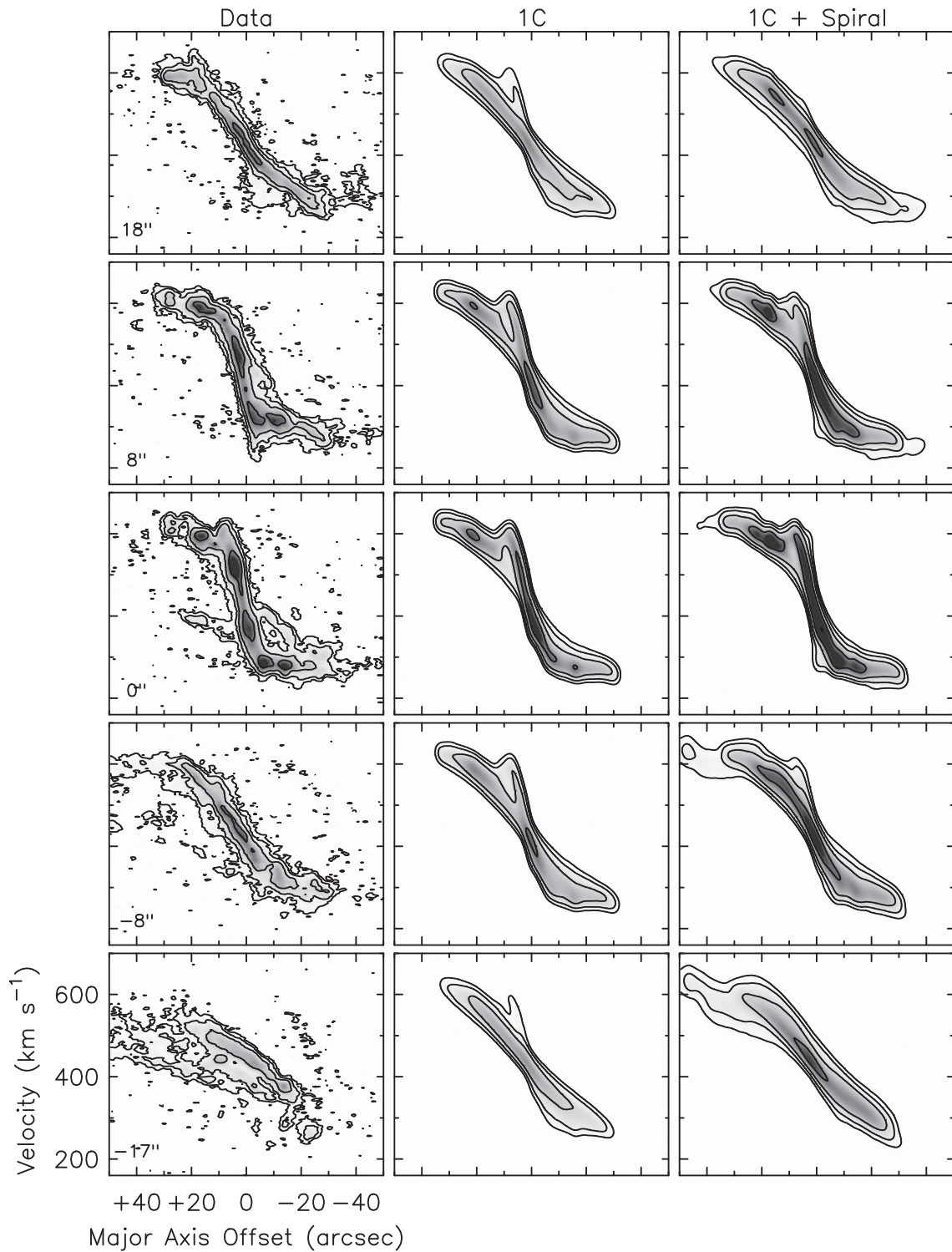


Figure 15. Position–velocity diagrams parallel to the major axis (lv diagrams) of the data, 1C, and 1C + spiral models. The material shifted toward systemic is almost entirely due to the streaming motions in the spiral arms. The blueshifted feature at $20''$ along the major axis corresponds to the southern disturbance. The component shifted closer to systemic from $0''$ to $-20''$ along the major axis corresponds to the northern stripe.

From the start it is clear that the fitting process is complicated by the presence of a bar and spiral arms extending from the center to the edge of the disk. Disk parameters for the final models are shown in Figure 14. The first (1C) model consists of only a single disk of constant inclination and position angle (column two of Figures 15 and 16). The second model (1C + spiral) consists of the same 1C disk model, but

with Gaussian distortions to reproduce the bar and spiral arms (column three of Figures 15 and 16). We retain symmetry whenever possible (i.e., modeling one side and then flipping it 180° to fit the other half before making as few alterations as possible). As may be expected, the bar and spiral arms appear to have some non-circular velocities. The orientation of the bar (i.e., directly along the direction of the expected outflow)

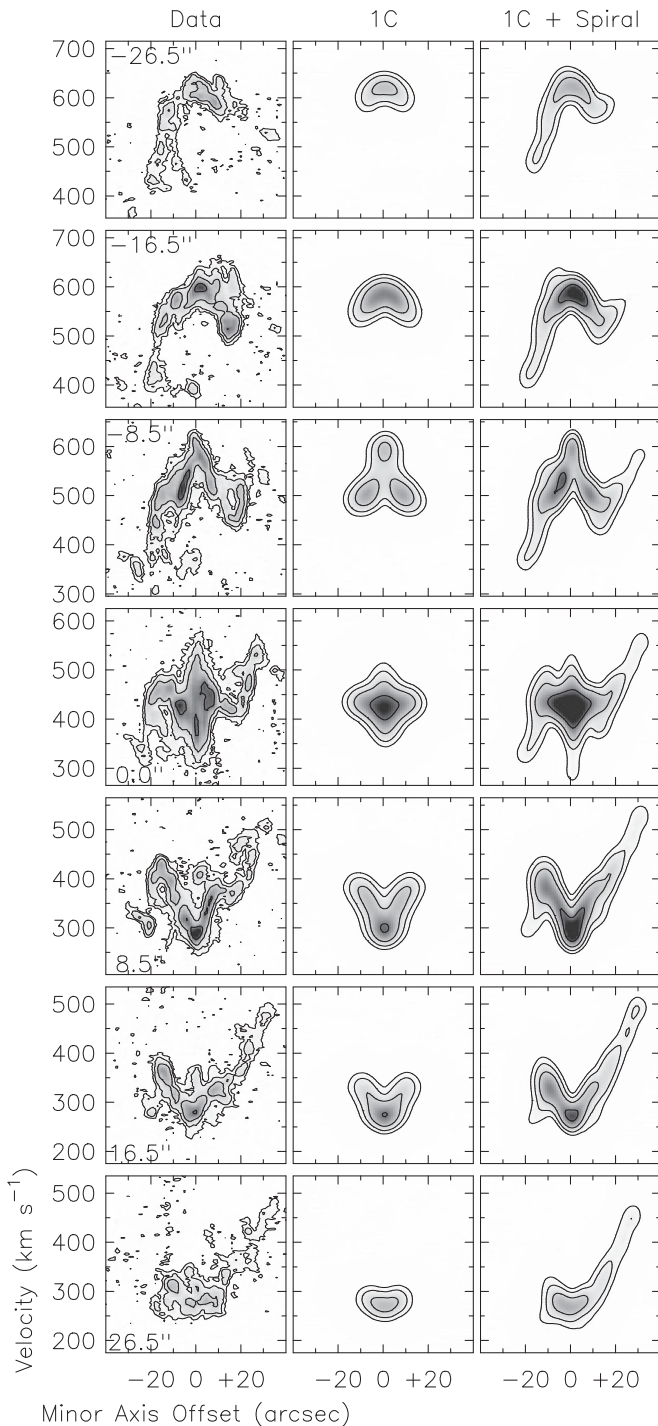


Figure 16. Position–velocity diagrams parallel to the minor axis (bv diagrams) of the data 1C, and 1C + spiral models. The stretching of features in velocity outside of $\pm 20''$ is due to large streaming motions in the spiral arms. Because of the non-circular velocities within the bar and (primarily outer) spiral arms, unambiguous outflow signatures cannot be extracted directly from these models.

makes it impossible to unambiguously distinguish between what is part of the bar and what is outflowing material. The innermost spiral arms exhibit primarily disk rotation. However, the velocities of the outermost spiral arms extending beyond the main disk are observed to be close to systemic for more than $20''$ (400 pc) along the length of each. If the rotation curve is matched to the main disk, a substantial radial inflow of

$100\text{--}150\text{ km s}^{-1}$ within the outer arms is the only way to reproduce the velocity field. Unfortunately, the precise details of these radial motions, rotational velocities, pitch-angle, and inclination are degenerate to some degree. The north-western arm intersects the location of the ionized outflow. With degenerate parameters for the spiral arms, it is not possible to reliably extract the molecular outflow in this region.

We obtain initial residuals and find indications of more material present in the overdense region, but nothing conclusive. We then use a more aggressive approach and oversubtract the models in order to eliminate virtually all material with disk rotation (thus also removing any outflow material that shares disk velocities). This approach does not yield any unambiguous detection of outflowing molecular gas either (Figure 9). While a similar approach has been applied to other galaxies (e.g., García-Burillo et al. 2014; Pereira-Santaella et al. 2016), yielding clear outflow signatures, it is not well-suited in the case of Circinus because of the shared disk and outflow velocities, as well as the orientation and non-circular motions of the bar and spiral arms.

The quality of the models is sufficient to demonstrate the extent to which this technique may be used to extract the outflow in Circinus. There are some minor imperfections in the spiral arms, but their fits would be degenerate in any case. It may be fruitful to perform an exhaustive modeling analysis in order to further constrain the streaming motions in the spiral arms and kinematics of the disk itself, but such an analysis is unrelated to the outflow and beyond the scope of this paper.

REFERENCES

- Aalto, S., Costagliola, F., Muller, S., et al. 2016, *A&A*, 590, A73
Aalto, S., García-Burillo, S., Muller, S., et al. 2015, *A&A*, 574, A85
Alatalo, K., Lacy, M., Lanz, L., et al. 2015, *ApJ*, 798, 31
Bacon, R., Accardo, M., Adjali, L., et al. 2010, *Proc. SPIE*, 7735, 773508
Barai, P., Viel, M., Borgani, S., et al. 2013, *MNRAS*, 430, 3213
Binney, J., & Tremaine, S. 2008, *Galactic Dynamics* (2nd ed.; Princeton, NJ: Princeton Univ. Press)
Bolatto, A. D., Warren, S. R., Leroy, A. K., et al. 2013a, *Natur*, 499, 450
Bolatto, A. D., Wolfire, M., & Leroy, A. K. 2013b, *ARA&A*, 51, 207
Booth, C. M., & Schaye, J. 2013, *NatSR*, 3, 1738
Briggs, D. 1995, PhD thesis, The New Mexico Institute of Mining and Technology
Caldú-Primo, A., & Schruba, A. 2016, *AJ*, 151, 34
Caldú-Primo, A., Schruba, A., Walter, F., et al. 2013, *AJ*, 146, 150
Cicone, C., Maiolino, R., Sturm, E., et al. 2014, *A&A*, 562, A21
Combes, F., García-Burillo, S., Casasola, V., et al. 2014, *A&A*, 565, A97
Contini, M., Prieto, M. A., & Viegas, S. M. 1998, *ApJ*, 505, 621
Dove, J. B., Shull, J. M., & Ferrara, A. 2000, *ApJ*, 531, 846
Elmouttie, M., Haynes, R. F., Jones, K. L., et al. 1998, *MNRAS*, 297, 1202
Faucher-Giguère, C.-A., & Quataert, E. 2012, *MNRAS*, 425, 605
Feruglio, C., Fiore, F., Carniani, S., et al. 2015, *A&A*, 583, A99
Feruglio, C., Maiolino, R., Piconcelli, E., et al. 2010, *A&A*, 518, L155
For, B.-Q., Koribalski, B. S., & Jarrett, T. H. 2012, *MNRAS*, 425, 1934
Freeman, K. C., Karlsson, B., Lynga, G., et al. 1977, *A&A*, 55, 445
García-Burillo, S., Combes, F., Usero, A., et al. 2014, *A&A*, 567, A125
Gentile, G., Józsa, G. I. G., Serra, P., et al. 2013, *A&A*, 554, A125
Greenhill, L. J., Booth, R. S., Ellingsen, S. P., et al. 2003, *ApJ*, 590, 162
Ho, I.-T., Medling, A. M., Bland-Hawthorn, J., et al. 2016, *MNRAS*, 457, 1257
Józsa, G. I. G., Kenn, F., Klein, U., & Oosterloo, T. A. 2007, *A&A*, 468, 731
Leroy, A. K., Walter, F., Decarli, R., et al. 2015a, *ApJ*, 811, 15
Leroy, A. K., Walter, F., Martini, P., et al. 2015b, *ApJ*, 814, 83
Maiolino, R., Krabbe, A., Thatte, N., & Genzel, R. 1998, *ApJ*, 493, 650
Marconi, A., Moorwood, A. F. M., Origlia, L., & Oliva, E. 1994, *Msngr*, 78, 20
Martin, C. L. 2005, *ApJ*, 621, 227
Matsushita, S., Muller, S., & Lim, J. 2007, *A&A*, 468, L49
Moorwood, A. F. M., Lutz, D., Oliva, E., et al. 1996, *A&A*, 315, L109
Morganti, R., Oosterloo, T., Oonk, J. B. R., et al. 2015, *A&A*, 580, A1
Morganti, R., Veilleux, S., Oosterloo, T., Teng, S. H., & Rupke, D. 2016, *A&A*, 593, A30

- Oliiva, E., Salvati, M., Moorwood, A. F. M., & Marconi, A. 1994, *A&A*, **288**, 457
- Oppenheimer, B. D., Davé, R., Kereš, D., et al. 2010, *MNRAS*, **406**, 2325
- Pawlik, A. H., & Schaye, J. 2009, *MNRAS*, **396**, L46
- Pereira-Santaella, M., Colina, L., García-Burillo, S., et al. 2016, arXiv:1607.03674
- Prieto, M. A., Reunanen, J., Tristram, K. R. W., et al. 2010, *MNRAS*, **402**, 724
- Rogstad, D. H., Lockhart, I. A., & Wright, M. C. H. 1974, *ApJ*, **193**, 309
- Sage, L. J., Henkel, C., & Mauersberger, R. 1991, *A&A*, **249**, 31
- Sakamoto, K., Aalto, S., Wilner, D. J., et al. 2009, *ApJL*, **700**, L104
- Salak, D., Nakai, N., Hatakeyama, T., & Miyamoto, Y. 2016, *ApJ*, **823**, 68
- Serra, P., Westmeier, T., Giese, N., et al. 2015, *MNRAS*, **448**, 1922
- Sharma, M., & Nath, B. B. 2012, *ApJ*, **750**, 55
- Sharp, R. G., & Bland-Hawthorn, J. 2010, *ApJ*, **711**, 818
- Siebenmorgen, R., Moorwood, A., Freudling, W., & Kaeufel, H. U. 1997, *A&A*, **325**, 450
- Somerville, R. S., Hopkins, P. F., Cox, T. J., et al. 2008, *MNRAS*, **391**, 481
- Stone, M., Veilleux, S., Meléndez, M., et al. 2016, *ApJ*, **826**, 111
- Sturm, E., González-Alfonso, E., Veilleux, S., et al. 2011, *ApJL*, **733**, L16
- Sturm, E., Verma, A., Graciá-Carpio, J., et al. 2010, *A&A*, **518**, L36
- Tadhunter, C., Morganti, R., Rose, M., Oonk, J. B. R., & Oosterloo, T. 2014, *Natur*, **511**, 440
- Tielens, A. G. G. M., & Hollenbach, D. 1985, *ApJ*, **291**, 722
- Tristram, K. R. W., Meisenheimer, K., Jaffe, W., et al. 2007, *A&A*, **474**, 837
- Tully, R. B., Rizzi, L., Shaya, E. J., et al. 2009, *AJ*, **138**, 323
- Veilleux, S., & Bland-Hawthorn, J. 1997, *ApJL*, **479**, L105
- Veilleux, S., Cecil, G., & Bland-Hawthorn, J. 2005, *ARA&A*, **43**, 769
- Veilleux, S., Meléndez, M., Sturm, E., et al. 2013, *ApJ*, **776**, 27
- Walter, F., Weiss, A., & Scoville, N. 2002, *ApJL*, **580**, L21
- Watanabe, Y., Sakai, N., Sorai, K., & Yamamoto, S. 2014, *ApJ*, **788**, 4
- Weilbacher, P. M., Streicher, O., Urrutia, T., et al. 2012, *Proc. SPIE*, **8451**, 84510B
- Weilbacher, P. M., Streicher, O., Urrutia, T., et al. 2014, in ASP Conf. Ser. 485, *Astronomical Data Analysis Software and Systems XXIII*, ed. N. Manset & P. Forshay (San Francisco, CA: ASP), 451
- Wilson, A. S., Shopbell, P. L., Simpson, C., et al. 2000, *AJ*, **120**, 1325
- Zhu, Y.-N., Wu, H., Cao, C., & Li, H.-N. 2008, *ApJ*, **686**, 155
- Zschaechner, L. K., & Rand, R. J. 2015, *ApJ*, **808**, 153
- Zschaechner, L. K., Rand, R. J., Heald, G. H., Gentile, G., & Józsa, G. 2012, *ApJ*, **760**, 37
- Zubovas, K., & King, A. 2012, *ApJL*, **745**, L34